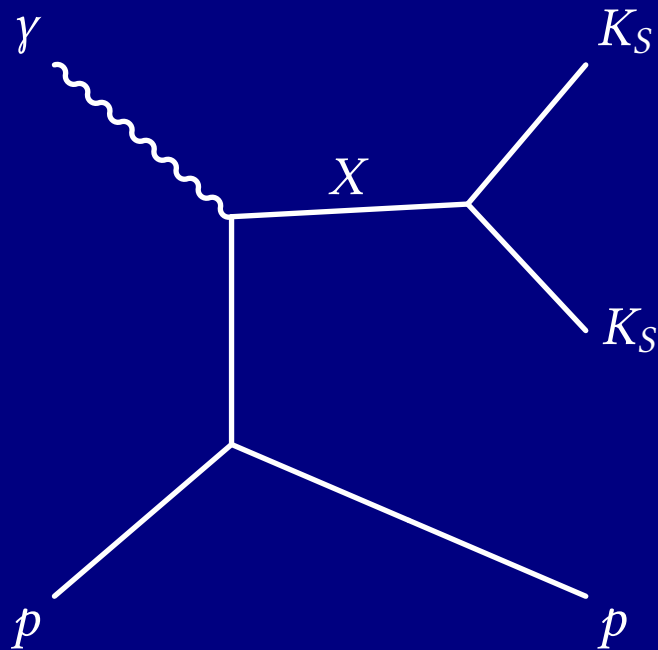


---

# PHOTOPRODUCTION OF $K_S$ PAIRS AT GLUEX

---



NATHANIEL DENE HOFFMAN

CARNEGIE MELLON UNIVERSITY

# Table of Contents

|          |   |           |
|----------|---|-----------|
| <b>1</b> | <b>Introduction</b>   | <b>1</b>  |
| 1.1      | A Brief History of Particle Physics . . . . .                 | 1         |
| 1.2      | Thesis Overview . . . . .                                     | 2         |
| 1.3      | Motivation . . . . .  | 2         |
| 1.4      | Past Analyses . . . . .                                       | 4         |
| <b>2</b> | <b>Experimental Design and Data Selection</b>                 | <b>7</b>  |
| 2.1      | The GlueX Experiment . . . . .                                | 7         |
|          | Particle Identification and the GlueX Kinematic Fit . . . . . | 11        |
| 2.2      | Data Selection for the $K_S K_S$ Channel . . . . .            | 16        |
|          | Fiducial Cuts . . . . .                                       | 16        |
| 2.3      | sPlot Weighting . . . . .                                     | 16        |
|          | Non-Factorizing sPlot . . . . .                               | 20        |
|          | Application of Weights . . . . .                              | 21        |
| <b>3</b> | <b>Partial-Wave Analysis</b>                                  | <b>27</b> |
| 3.1      | Amplitude Formalism . . . . .                                 | 27        |
|          | Single-Particle Helicity States . . . . .                     | 27        |
|          | Two-Particle Helicity States . . . . .                        | 29        |
|          | Production Amplitudes . . . . .                               | 31        |
|          | Including Linear Photon Polarization . . . . .                | 32        |
| 3.2      | The $Z_\ell^m$ Amplitude . . . . .                            | 34        |
| 3.3      | The $K$ -Matrix Parameterization . . . . .                    | 37        |
|          | Resonances as Poles of the $K$ -matrix . . . . .              | 39        |
| 3.4      | Waveset Selection . . . . .                                   | 43        |

|          |                                       |           |
|----------|---------------------------------------|-----------|
| <b>4</b> | <b>Results and Systematic Studies</b> | <b>45</b> |
| 4.1      | Fitting Methods . . . . .             | 45        |
|          | Uncertainty Estimation . . . . .      | 48        |
| 4.2      | Mass-Independent Fits . . . . .       | 50        |
| 4.3      | Mass-Dependent Fits . . . . .         | 50        |
| 4.4      | Systematics . . . . .                 | 50        |
| <b>5</b> | <b>Conclusion</b>                     | <b>51</b> |
|          | <b>Bibliography</b>                   | <b>53</b> |



# Chapter 1

## Introduction

### 1.1 A Brief History of Particle Physics

Since the days of the ancient Greeks, scientists and philosophers alike have been interested in the fundamental question concerning the composition of the universe. While some Greeks maintained that the world was composed of four indivisible elemental substances (fire, earth, air, and water) [1], this was at best a guess by the early philosophers, who had no mechanism with which to test their theory. Ironically, these philosophers struggled with a question to which us modern physicists still have no answer: Are the building blocks of the natural world fundamental (indivisible) [2]?

In 1808, John Dalton published a manuscript which described what is now called the "law of multiple proportions" after compiling several observations on chemical reactions which occur with specific proportions of their reactants. He anglicized the Greek *atomos*, meaning "not able to be cut", into the word we are familiar with—"atom" [3]. Towards the end of the century, J. J. Thomson demonstrated that cathode rays could be deflected by an electromagnetic field, an observation which could not be explained by the prevailing theory that the rays were some form of light [4]. Instead, he proposed that these rays were made up of charged particles he called "corpuscles" (later renamed to the familiar "electrons") [5]. Around the same time (between 1906 and 1913), Ernest Rutherford, Hans Geiger, and Ernest Marsden conducted experiments in which they scattered alpha particles through a thin metal foil, and, through an analysis of the scattering angles, concluded that a positively charged nucleus must exist at the center of atoms, surrounded by electrons [6].

Over the next several decades, the nucleus was further divided into protons and neutrons<sup>1</sup> [7, 8]. In 1964, Murray Gell-Mann and George Zweig proposed a theory that protons and neutrons (and all other baryons and mesons) were in fact composed of smaller particles Gell-Mann called "quarks" [9]. These particles, along with the electron-like

---

<sup>1</sup>For the discovery of the electron and neutron, Thomson and James Chadwick won Nobel Prizes in Physics in 1906 and 1935, respectively. Rutherford won the 1908 Nobel Prize in Chemistry for his research in radiation. However, I want to emphasize that while I mention the "big names" here, there are many who contributed in relative obscurity.

family of leptons (including neutrinos), the gauge bosons, and the Higgs boson, discovered in 2012 [10], comprise elements of the Standard Model, a mathematical model which describes all the known forces and matter of the universe, with the notable exceptions (at time of writing) of gravity, dark matter, dark energy, and neutrino masses.

This thesis begins at a time when physicists are working hard to find gaps in this model, mostly by probing higher and higher ranges of energy. The experimental work being done at GlueX, however, resides in a lower energy regime, which we usually describe as “medium energy physics”. As I will elucidate later in this manuscript, the strong force is non-perturbative in this regime, making direct calculations through the Standard Model all but impossible. However, since the advent of Lattice Quantum Chromodynamics (LQCD) in 1974 [11], physicists have been able to make approximate predictions via computer simulations of the theory.

## 1.2 Thesis Overview

Herein, I will focus on a particular portion of the Standard Model that dictates the strong interaction, viz. interactions between quarks and gluons, the mediating gauge boson of the strong force. Beginning with a discussion of the theory and history of  $K_S$  (K-short) pair production in prior experiments, I will give a brief overview of the GlueX experiment. I will then outline some of the theoretical underpinnings and implications of glueballs to persuade the reader of the importance of this production channel in the larger scheme of GlueX.

Next, I will describe my own analysis, beginning with the the impetus of this study, a search for  $\Sigma^+$  baryons using a different recombination of the final state in this channel. We will then turn our attention to the many resonances which decay to  $K_S$  pairs, and I will delineate the layers of data selection which have been carried out to produce a clean sample of events.

I will then discuss the process of partial-wave analysis (PWA), modeling resonances, and selecting a waveset for my data. I will conclude with the results from fits of these models to the data, the implications of such fits, and the next steps which I or another particle physicist might take in order to illuminate another corner of the light mesonic spectrum.

## 1.3 Motivation

While this will be discussed in detail later, I believe it is important to emphasize the motivation for such a study of photoproduction of  $K_S K_S$ . While the majority of GlueX research concerns the search for hybrid mesons (mesons with valence gluons which contribute to their angular momentum, including “exotic” mesons with quantum numbers forbidden by  $q\bar{q}$ -only states), such mesons cannot be found in this channel. Given a bound state of two spin- $\frac{1}{2}$  quarks with relative angular momentum  $L$ , total spin  $S$  and total angular momentum  $J$  (the eigenvalue of  $\hat{J}^2 = \hat{L}^2 \oplus \hat{S}^2$ ), we

can define the parity operator  $\hat{P}$  by its effect on the wave function of the system,

$$\hat{P}|\vec{r}\rangle = \eta|\vec{r}\rangle \quad (1.1)$$

where  $\eta$  can be determined by noting that states of angular momentum are generally proportional to a spherical harmonic in their angular distribution ( $|r, \theta, \varphi; LM\rangle \sim Y_L^M(\theta, \varphi)$ ) and

$$\hat{P}Y_L^M(\theta, \varphi) = Y_L^M(\pi - \theta, \pi + \varphi) = (-1)^L Y_L^M(\theta, \varphi) \quad (1.2)$$

so  $\eta = (-1)^L$ . The Dirac equation can be used to show that the intrinsic parity of quarks and antiquarks, when multiplied, yields a factor of  $-1$ , so

$$\hat{P}|q\bar{q}; J L M S\rangle = -(-1)^L \quad (1.3)$$

Similarly, the charge-conjugation operator  $\hat{C}$  (also called C-parity) will introduce a factor of  $(-1)^L$  because exchanging charges of a (neutral<sup>2</sup>) quark-antiquark system is akin to reversing their positions under parity. If  $|S\rangle$  is antisymmetric under C-parity, we should get an additional factor of  $-1$ , which is the case for the  $S = 0$  singlet. With the aforementioned  $-1$  due to the intrinsic parity of the quarks and antiquarks, we find

$$\hat{C}|q\bar{q}; J L M S\rangle = (-1)^{L+S} \quad (1.4)$$

Labeling states with the common  $J^{PC}$  notation, it can then be shown that states like  $0^{--}$ ,  $0^{+-}$ ,  $1^{+-}$ , and  $2^{+-}$  (among others) are not allowed states for  $q\bar{q}$  mesons. As mentioned, the search for such states is a main focus of the GlueX experiment. However, since the particles we are concerned with decays to two identical mesons ( $K_S$ ) which have a symmetric spatial wave function, and because these particles are mesons which follow Bose-Einstein statistics, the angular part of the total wave function must also be symmetric, i.e.  $J = \text{even integers}$ . Furthermore, because parity is conserved in strong decays, and the state of two identical particles is symmetric under parity, the decaying mesons must also have  $P = +$ . Finally, the strong interaction also conserves C-parity, and both kaons are neutral, so we can determine the  $J^{PC}$  quantum numbers of the resonance to be even<sup>++</sup>. There should be no overlap here with the aforementioned exotic mesons, but that does not mean the channel is not of interest to GlueX and the larger scientific community. Particularly, the lowest lying glueball states are predicted to not only share these quantum numbers, but exist in the middle of the mass range produced by GlueX energies[12]. To add to this, the spin-0 isospin-0 light flavorless mesons, denoted as  $f_0$ -mesons, may be supernumerary, either due to mixing with a supposed light scalar glueball or by the presence of a light tetraquark or hybrid states (or both)[13].

However, it would be an understatement to say that the  $K_S K_S$  channel at GlueX is not the ideal place to be looking for hybrids, glueballs or tetraquarks. This is because, while we have excellent handles for reconstructing

---

<sup>2</sup>For  $\hat{C}$  to be Hermitian, and thus observable, acting it twice on a state should return the original state, so only eigenvalues of  $\pm 1$  are allowed. Therefore, only states which are overall charge neutral are eigenstates of  $\hat{C}$ .

this channel, we have no ability to separate particles of different isospin with these data alone. This means that these  $f$  states will be indistinguishable from their isospin-1 partners, the  $a$ -mesons. At first glance, it might seem like a model of the masses of these particles would make it easy to separate them, even if they remained indistinguishable between resonant peaks, but with broad states like the  $f_0(1370)$  and states which sit right on top of each other (like the  $f_0(980)$  and  $a_0(980)$ , which also tend to interfere with each other), there is likely no unique mass model which can distinguish all of the possible states without relying on data from other channels.

The silver lining is that, due to the GlueX detector’s state-of-the-art angular acceptance[14], we do stand a chance at separating spin-0 states from spin-2 states, and GlueX’s polarized beam allows us to further understand the mechanisms at play by giving us some indication of the parity of the  $t$ -channel exchanged particle in the production interaction. We can also use this channel as a proving ground for more complex amplitude analysis involving a mass model, which could be extended to a coupled-channel analysis in the future.

## 1.4 Past Analyses

The present work is certainly not the first attempt to study  $K_S^0$  pair production. The earliest published experiment with a similar final state dates back to 1961, where researchers at CERN measured 54 events which ended in a final state which included two neutral kaons<sup>3</sup>. For the majority of the 1960s and 1970s, research into this final state was dominated by pion beam production off a proton target, aside from one kaon beam experiment in 1977 (see Table 1.1). In the 1980s, several collaborations at DESY began studying electron-positron collisions, which imply an internal virtual photon fusion as the production mechanism. These experiments are an important counterpoint to those involving hadrons, since the glueball does not couple to photons, so any intermediate glueball production in these reactions should be heavily suppressed [15], although radial excitations of any glueballs should couple [16]. While the statistical power of these experiments was very small at first (relative to pion beam experiments), the L3 collaboration at LEP and Belle at KEKB provided larger data samples in the first two decades of the 2000s. Until this study, ITEP and BNL held the statistical lead in non-photon-fusion experiments, and we now present a dataset which is larger than both, even using the most restrictive selections of data.

There has only been one prior experiment, published by the CLAS collaboration in 2018 [17], which used photoproduction as a means of accessing this channel. While the “golden channel” for glueball production remains radiative  $J/\psi$  decays to  $K_S^0 K_S^0 \gamma$ , since non-glueball intermediate processes converting charm quarks into strange quarks are suppressed, photoproduction could be effective at creating exotic hybrid states as well as glueballs via the photon’s hadronic component or Pomeron exchange [16]. Additionally, the CLAS experiment did not utilize the polarized photon beam capability at JLab, but the current analysis at GlueX does, and this access to linear photon

---

<sup>3</sup>Since only  $K_S^0$  eigenstates decayed inside the bubble chamber, while the longer lived  $K_L^0$  would typically decay somewhere outside the chamber, these experiments inferred a final state of  $K_S^0 K_S^0$ . The same can be said for modern experiments, including GlueX.



| Channel   | Collaboration | # Events           | Year                  |
|---|---------------|--------------------|-----------------------|
| $\pi^- p \rightarrow K_S^0 K_S^0 n$                 | CERN/PS       | 54                 | 1961 [18]             |
| $\pi^- p \rightarrow K_S^0 K_S^0 n$                 | BNL           | 19                 | 1962 [19]             |
| $\pi^- p \rightarrow K_S^0 K_S^0 n$                 | LRL           | 66                 | 1962 [20]             |
| $\pi^- p \rightarrow K_S^0 K_S^0 + \text{neutrals}$ | BNL           | 374                | 1966 [21]             |
| $\pi^- p \rightarrow K_S^0 K_S^0 n$                 | LRL           | 426                | 1966 [22]             |
| $\pi^- p \rightarrow K_S^0 K_S^0 n$                 | LRL           | 418                | 1967 [23]             |
| $\pi^- p \rightarrow K_S^0 K_S^0 n$                 | CERN/PS       | 2559               | 1967 [24]             |
| $\pi^- p \rightarrow K_S^0 K_S^0 n$                 | ANL/ZGS       | 1969               | 1968 [25] & 1969 [26] |
| $\pi^- p \rightarrow K_S^0 K_S^0 n$                 | CERN/PS       | 4820               | 1975 [27]             |
| $\pi^- p \rightarrow K_S^0 K_S^0 n$                 | CERN/PS       | 6380               | 1976 [28]             |
| $\pi^- p \rightarrow K_S^0 K_S^0 n$                 | ANL/ZGS       | 5096               | 1976 [29] & 1979 [30] |
| $K^- p \rightarrow K_S^0 K_S^0 + \text{neutrals}$   | CERN/PS       | 410                | 1977 [31]             |
| $\pi^- p \rightarrow K_S^0 K_S^0 n$                 | BNL/MPS       | 1278               | 1980 [32]             |
| $\pi^- p \rightarrow K_S^0 K_S^0 n$                 | BNL/MPS       | 29381              | 1982 [33]             |
| $e^+ e^- \rightarrow e^+ e^- K_S^0 K_S^0$           | DESY/TASSO    | 100                | 1983 [34]             |
| ???   | ???           | ???                | 1986 (Bolonkin)       |
| ???   | ???           | ???                | 1986 (Baloshin)       |
| $\pi^- p \rightarrow K_S^0 K_S^0 n$                 | BNL/MPSII     | 40494              | 1986 [35]             |
| $e^+ e^- \rightarrow e^+ e^- K_S^0 K_S^0$           | DESY/PLUTO    | 21                 | 1987 [36]             |
| $K^- p \rightarrow K_S^0 K_S^0 \Lambda$             | SLAC/LASS     | 441                | 1988 [37]             |
| $e^+ e^- \rightarrow e^+ e^- K_S^0 K_S^0$           | DESY/CELLO    | 26                 | 1988 [38]             |
| $e^+ e^- \rightarrow e^+ e^- K_S^0 K_S^0$           | LEP/L3        | 62                 | 1995 [39]             |
| $pp \rightarrow pp K_S^0 K_S^0$                     | Fermilab/E690 | 11182              | 1998 [40]             |
| $\pi^- p \rightarrow K_S^0 K_S^0 + \text{neutrals}$ | ITEP          | 1000 <sup>†</sup>  | 1999 [41]             |
| $e^+ e^- \rightarrow e^+ e^- K_S^0 K_S^0$           | LEP/L3        | 802                | 2001 [15]             |
| $\pi^- C \rightarrow K_S^0 K_S^0 + X$               | ITEP          | 553                | 2003 [42]             |
| $e^+ e^- \rightarrow e^+ e^- K_S^0 K_S^0$           | LEP/L3        | 870                | 2006 [43]             |
| $\pi^- p \rightarrow K_S^0 K_S^0 n$                 | ITEP          | 40553              | 2006 [44]             |
| $e^+ e^- \rightarrow e^+ e^- K_S^0 K_S^0$           | KEKB/Belle    | ???                | 2013 [45]             |
| $\gamma p \rightarrow K_S^0 K_S^0 p$                | JLAB/CLAS     | 13500 <sup>‡</sup> | 2018 [17]             |
| $\gamma p \rightarrow K_S^0 K_S^0 p$                | JLAB/GlueX    | 65468*             | 2025 (this analysis)  |

**Table 1.1:** Summary of all (known) past analyses involving production of  $K_S^0$  pairs. Note that this is possibly not exhaustive and does not include any studies which focus on decays of an intermediate state, i.e.  $J/\psi \rightarrow \gamma K_S^0 K_S^0$ .

<sup>†</sup> - Estimated from plots.

<sup>‡</sup> - Reported as three orders of magnitude larger than LEP's result from 2006, but an exact count was difficult to estimate.

\* - Weighted number of events with  $\text{KinFit } \chi_v^2 < 3.0$ , the most restrictive selection used in this analysis (see [Sections 2.1](#) and [2.2](#)).

polarization can inform us of the parity exchanged in production of such exotic states. Our dataset is at least 4.8× larger than what was used in the CLAS measurement.



## Chapter 2

# Experimental Design and Data Selection

### 2.1 The GlueX Experiment

GlueX, short for the Gluonic Excitation experiment located at the Thomas Jefferson National Accelerator Facility (JLab), first began collecting publication-quality data in 2016 with the goal of establishing the spectrum of light mesonic states including hybrid mesons and glueballs.

GlueX receives an unpolarized electron beam from the Continuous Electron Beam Accelerator Facility (CEBAF), which is then converted to linearly polarized photons via coherent bremsstrahlung from a diamond radiator (see Figure 2.1). The scattering electrons are detected in an array of high-resolution scintillators called the Tagger Mi-

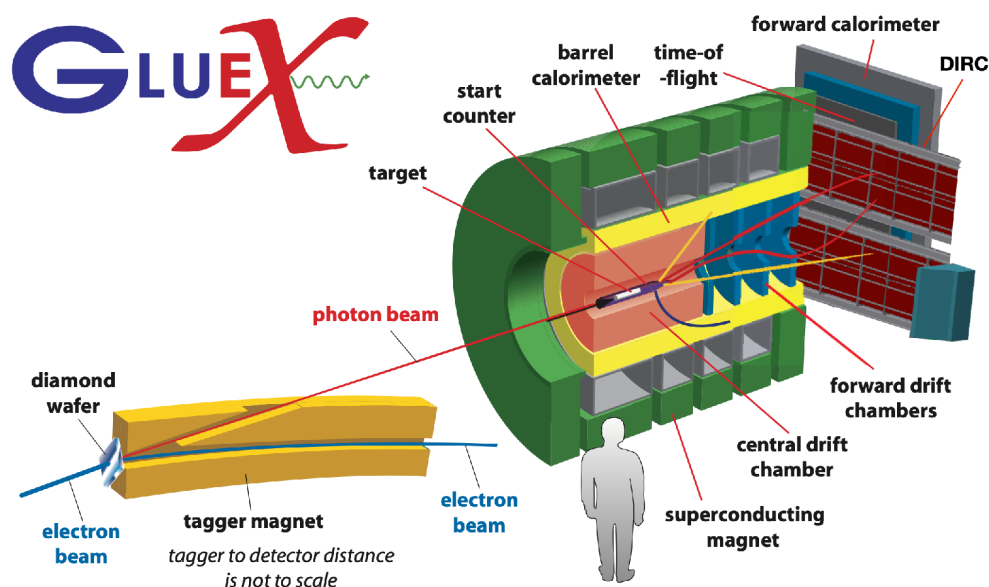


**Figure 2.1:** A diagram of the GlueX detector at JLab. The DIRC detector was installed in 2019 and was only present for about half of the data analyzed in this study.[CITE](#)

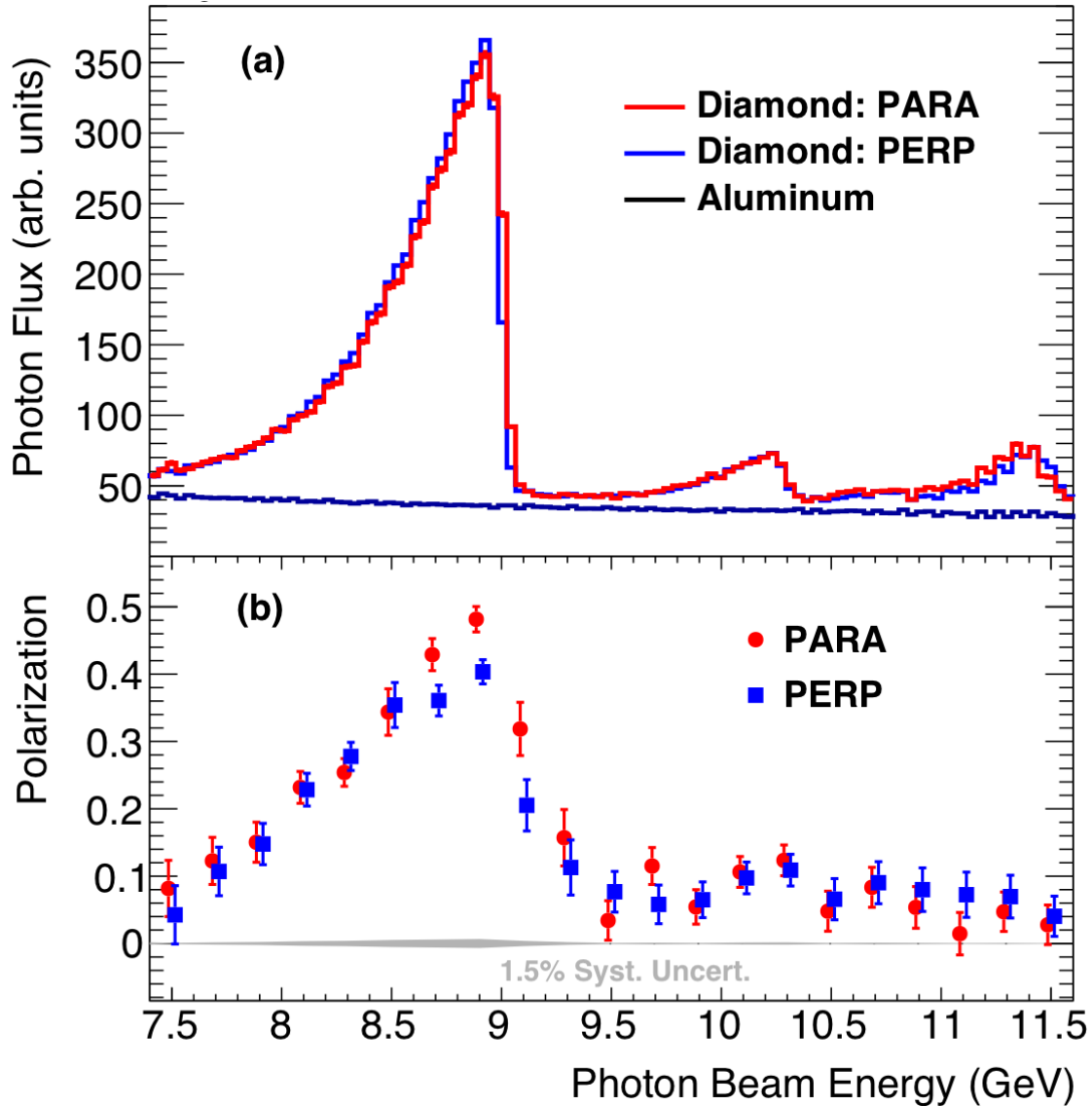


**Figure 2.2:** (a) Collimated photon beam intensity versus energy as measured by the Pair Spectrometer. (b) Collimated photon beam polarization as a function of beam energy, as measured by the Triplet Polarimeter, with data points offset horizontally by  $\pm 0.015$  GeV for clarity. The labels PARA and PERP refer to orientations of the diamond radiator that result in polarization planes that are parallel and perpendicular to the horizontal, respectively (figure and caption from [14]).

croscop (TAGM) which covers beam energies between 8 and 9 GeV, a region of energy referred to as the “coherent peak”. The orientation of the diamond radiator is optimized to produce the highest photon polarization and flux in this region (see Figure 2.2). The rest of the energy range, regions from about 3–8 GeV and 9–12 GeV, are covered by the lower-resolution Tagger Hodoscope (TAGH). These elements are used to determine only the photon energy, which is equal to the difference between the incident and outgoing electron energies [14].

To measure the polarization properties of the photon beam as well as the photon flux, the photon beam passes through a thin beryllium foil which induces  $e^+e^-$  pair production on some known fraction of the photons (see Fig-

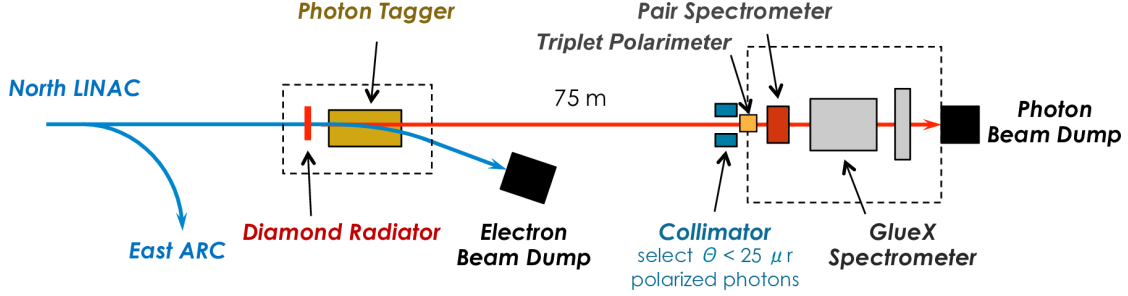


**Figure 2.3:** A diagram of the beamline layout of the Triplet Polarimeter (TPOL) and Pair Spectrometer (PS) used to measure the polarization and beam flux.

ure 2.3). The angular distribution of the produced electrons along with an electron knocked out of the foil medium as part of the pair production process is measured by the Triplet Polarimeter (TPOL) to determine the photon polarization fraction. The Pair Spectrometer (PS) then counts the pair-produced electrons in coincidence with the TAGM and TAGH detectors. A known fraction<sup>1</sup> of the beam is converted to  $e^+e^-$  pairs in this way, allowing for an accurate measurement of the photon flux and the energy dependence of the polarization fraction.

Photons which do not pair-produce in the beryllium radiator interact with a liquid hydrogen cryotarget, which maintains a temperature of 20.1 K, allowing the contents to act as a stationary proton target. A set of thin scintillators called the Start Counter (ST) surrounds the target, which captures the initial signals (and azimuthal angles) from reaction products and associates them with the electron radio frequency (RF) beam bunch from which the reaction originated<sup>2</sup>. Any products of the reaction next pass through either the Central Drift Chamber (CDC) or Forward Drift Chamber (FDC) depending on their trajectory (particles within  $1^\circ$ – $10^\circ$  of the beamline pass through the FDC, and the detector has partial coverage up to  $20^\circ$ ). The CDC is filled with long metal tubes at various orientations, while the FDC chambers are flat disks. Each tube/disk is filled with a gaseous mixture of argon and carbon dioxide<sup>3</sup> with a thin wire running through their center of each tube and an array of wires crossing the plane of each disk. The wire and tube/disk faces are held at a voltage differential, and charged particles passing through the chambers ionize

<sup>1</sup>We know the radiation length of the beryllium foil, and this along with the radiator thickness determines the fraction of photons which will pass through without interacting.

<sup>2</sup>The electron beam bunches from the CEBAF arrive every 4 ns, a rate of 250 MHz.

<sup>3</sup>These particular gases and the mixture ratio are chosen to reduce interfering effects from the magnetic field of the main solenoid.

the gases inside. The faster-moving electrons move towards the positively charged wires, while the slower-moving ions move towards the tubes/disks. The combination of these signals allows for the reconstruction of the trajectories of each charged particle which passes through each chamber. Both detectors are situated inside a solenoid with a magnetic field around 2 T, and this field bends the trajectories of charged particles, allowing for proper identification of the sign of the charge as well as the particle’s momentum.

The Barrel Calorimeter (BCAL) surrounding the CDC and the Forward Calorimeter (FCAL) in front of the FDC measure the energy of electromagnetic deposits from interactions with charged and neutral particles. This includes photons originating from the decays of light neutral mesons like the  $\pi^0$  and  $\eta$ . Because such neutral particles pass through the CDC and FDC without detection, these calorimeters are necessary for their reconstruction. However, since there are no intermediate trajectories, GlueX is unable to reconstruct the decay vertices of these neutral particles. Since we are studying a reaction with a fully charged final state, this might not seem important. However, in [Section ?](#), we will discuss the study of neutral decays of  $K_S^0 \rightarrow 2\pi^0 \rightarrow 4\gamma$ , where the reconstruction will be severely limited due to the inability to reconstruct the decay vertex of the  $K_S^0$ .

There is a final scintillator array called the Time-of-Flight (TOF) detector situated immediately between the FDC and the FCAL. In combination with the ST and the RF timing information from the accelerator, this aids in charged-particle identification via a measurement of the flight time between the two detectors. Additionally, in 2019, an additional detector, the DIRC<sup>4</sup> detector was installed between the TOF and FDC to further aid in identification of charged pions and kaons. This detector measures the angle of the cone of Cherenkov radiation emitted by relativistic charged particles, which can be used to ascertain their velocity via the relation  $\cos \theta_c \sim 1/v$ . When compared to measurements of the particle’s momentum, this detector can be used to distinguish pions, kaons, and protons. Further information about the GlueX detector and the DIRC can be found in references [14] and [46] respectively.

The data analyzed in this thesis were collected in four separate “run periods” across two experiment “phases”, denoted Phase-I and Phase-II. Phase-I consists of three run periods, notated Spring 2017, Spring 2018, and Fall 2018 by the season and year when data collection began, and Phase-II contains one run period, Spring 2020<sup>5</sup> and is the only dataset which was collected after the DIRC installation. The total luminosity, coherent peak range, and luminosity in the coherent peak for each run period is listed in [Table 2.1](#).

The entire GlueX detector has been simulated with Geant4. Due to small changes and updates to the detector and its simulation between run periods, we will treat these datasets separately during the analysis, only presenting combined results in summary. Therefore, when generating Monte Carlo simulated data to model detector acceptance, each run period must be simulated separately.

---

<sup>4</sup>An acronym for Detection of Internally Reflected Cherenkov light

<sup>5</sup>This run technically began at the end of 2019

| Experiment | Run Period  | Luminosity ( $E_\gamma > 6.0$ GeV) | Coherent Peak Range | Luminosity in Coherent Peak |
|------------|-------------|------------------------------------|---------------------|-----------------------------|
| Phase-I    | Spring 2017 | 74.7 pb <sup>-1</sup>              | 8.2–8.8 GeV         | 21.8 pb <sup>-1</sup>       |
|            | Spring 2018 | 223.8 pb <sup>-1</sup>             | 8.2–8.8 GeV         | 63.0 pb <sup>-1</sup>       |
|            | Fall 2018   | 141.1 pb <sup>-1</sup>             | 8.2–8.8 GeV         | 40.1 pb <sup>-1</sup>       |
| Phase-II   | Spring 2020 | 386.2 pb <sup>-1</sup>             | 8.0–8.6 GeV         | 132.4 pb <sup>-1</sup>      |
| Total      |             | 825.8 pb <sup>-1</sup>             |                     | 257.3 pb <sup>-1</sup>      |

**Table 2.1:** Summary of total luminosity and total luminosity in the coherent peak for each run period.

### Particle Identification and the GlueX Kinematic Fit

Data collected from the GlueX detector mostly contains reaction topologies (the set of initial-, intermediate-, and final-state particles) which are not the channel of interest in this thesis, as the GlueX experiment uses a broad trigger to collect data with a wide range of final states. Additionally, due to the unavoidable finite resolution of each detector, the measured quantities such as the momentum of each particle might not exactly align with physical expectations (such as four-momentum conservation). For these reasons, we need to filter the detected data to just events which match our desired topology and kinematically fit the observables such as particle masses, decay vertices, and four-momenta with constraints that enforce conservation laws and other properties of interest.

This process begins with particle reconstruction, where the raw detector data is transformed into charged particle tracks (from the drift chambers), electromagnetic showers (from the calorimeters), and timing data from the ST, TOF, and accelerator RF signal. Next, the charged tracks are matched up with their respective showers from the calorimeters, and the remaining showers are labeled as “neutral showers” originating from photons (or possibly neutral particles like neutrons). At this stage, no particle identification is assigned to the charged and neutral tracks. Track reconstruction is performed before data is “skimmed” (separated into final-state topologies) so that all GlueX datasets are processed in the same way. My own analysis and data selection happens after track reconstruction, particle identification cuts, and the kinematic fit, after which there are still many events which likely belong to backgrounds which make it through these steps.

### Particle Identification Cuts

The next stage involves filtering through reconstructed tracks to find candidate events which match our topology. Timing cuts are applied to whichever detector gives the best timing information (the order being BCAL, TOF, FCAL, ST). By timing, we mean the difference between the time measured in the detector and the time of the RF beam bunch measured in the TAGH/TAGM. Each set of charged tracks is identified with each charged particle in the topology (events with too many or too few charged tracks are excluded). Each hypothetical identification is then subjected to cuts on the energy lost in the drift chambers or deposited in the calorimeters. Since there are no “missing” final-state

| Particle  | Selected Values                                    | Unit   | Detector |
|-----------|--|--|----------|
| $\gamma$  | $-1.5 \leq \Delta t_{\text{RF}} \leq 1.5$          | ns   | BCAL     |
|           | $-2.5 \leq \Delta t_{\text{RF}} \leq 2.5$          | ns   | FCAL     |
|           | $-0.1 \leq \text{MM}^2 \leq 0.1$                   | $(\text{GeV}/c^2)^2$                           | N/A      |
| $\pi^\pm$ | $-1.0 \leq \Delta t_{\text{RF}} \leq 1.0$          | ns   | BCAL     |
|           | $-0.5 \leq \Delta t_{\text{RF}} \leq 0.5$          | ns   | TOF      |
|           | $-2.0 \leq \Delta t_{\text{RF}} \leq 2.0$          | ns   | FCAL     |
|           | $-2.5 \leq \Delta t_{\text{RF}} \leq 2.5$          | ns   | ST       |
|           | $\frac{dE}{dx} < \exp[-7.0 \vec{p}  + 3.0] + 6.2$  | keV/cm $(\frac{dE}{dx})$ , GeV/c $( \vec{p} )$ | CDC      |
|           | $-1.0 \leq \text{MM}^2 \leq 1.0$                   | $(\text{GeV}/c^2)^2$                           | N/A      |
| $p$       | $-1.0 \leq \Delta t_{\text{RF}} \leq 1.0$          | ns   | BCAL     |
|           | $-0.6 \leq \Delta t_{\text{RF}} \leq 0.6$          | ns   | TOF      |
|           | $-2.0 \leq \Delta t_{\text{RF}} \leq 2.0$          | ns   | FCAL     |
|           | $-2.5 \leq \Delta t_{\text{RF}} \leq 2.5$          | ns   | ST       |
|           | $\frac{dE}{dx} > \exp[-4.0 \vec{p}  + 2.25] + 1.0$ | keV/cm $(\frac{dE}{dx})$ , GeV/c $( \vec{p} )$ | CDC      |
|           | $-0.5 \leq \text{MM}^2 \leq 4.41$                  | $(\text{GeV}/c^2)^2$                           | N/A      |
| $\pi^0$   | $0.08 \leq \text{IM} \leq 0.19$                    | GeV/c <sup>2</sup>                             | N/A      |
|           | $-1.0 \leq \text{MM}^2 \leq 1.0$                   | $(\text{GeV}/c^2)^2$                           | N/A      |
| $K_S^0$   | $0.3 \leq \text{IM} \leq 0.7$                      | GeV/c <sup>2</sup>                             | N/A      |
|           | $-1.0 \leq \text{MM}^2 \leq 2.0$                   | $(\text{GeV}/c^2)^2$                           | N/A      |
| N/A       | $-3.0 \leq \text{ME} \leq 3.0$                     | GeV  | N/A      |

**Table 2.2:** PID cuts used in event reconstruction.  $\text{MM}^2$  corresponds to the missing mass squared, IM corresponds to the invariant mass, and  $\text{ME}$  corresponds to the total missing energy.

particles (such as a neutron) in our reaction, an additional cut is made on the missing energy (the difference between the initial energy from the beam photon and the summed energy of the detected final-state particles). Finally, cuts are made on the invariant mass of some particles, as well as the missing mass (squared) of the entire reaction (the squared difference in invariant mass between the initial and final state). A summary of these particle identification (PID) cuts can be seen in [Table 2.2](#).

### Kinematic Fit

The final stage of reconstruction invokes a kinematic fit (KinFit) over data which has passed all separate PID cuts. The general structure of the kinematic fit is underpinned by the following derivation from [\[?\]](#)<sup>6</sup>. This kinematic fit minimizes the following objective function:

$$\chi^2(\vec{\eta}, \vec{\xi}) = (\vec{y} - \vec{\eta})^T \mathbf{V}_{\vec{y}}^{-1} (\vec{y} - \vec{\eta}) + 2\vec{\lambda}^T \vec{f}(\vec{\eta}, \vec{\xi}) \quad (2.1)$$

where  $\vec{y}$  are the experimentally measured values of observables  $\vec{\eta}$ ,  $\mathbf{V}_{\vec{y}}$  is the covariance matrix of the measured  $\vec{y}$ ,  $\vec{f}(\vec{\eta}, \vec{\xi}) = 0$  are constraints applied to the system with additional free parameters  $\vec{\xi}$  (which do not correspond to

<sup>6</sup>How to cite GlueX docdb 2112?



measured observables), and  $\lambda$  are unknown Lagrange multipliers for said constraints. For example,  $\vec{y}$  could include the measured four-momenta of all initial- and final-state particles, and  $\mathbf{V}_{\vec{y}}$  would describe the uncertainty (from the detector elements) of each measurement. One possible constraint function  $\vec{f}$  might minimize the difference between the initial and final four-momentum, as in Equation (2.12). Since we wish to minimize  $\chi^2$ , we first take derivatives with respect to each set of free parameters,

$$\frac{\partial \chi^2}{\partial \vec{\eta}} = \mathbf{V}_{\vec{y}}^{-1}(\vec{\eta} - \vec{y}) + \left( \frac{\partial \vec{f}}{\partial \vec{\eta}} \right)^{\top} \vec{\lambda} \quad (2.2)$$

$$\frac{\partial \chi^2}{\partial \vec{\lambda}} = \vec{f}(\vec{\eta}, \vec{\xi}) \quad (2.3)$$

$$\frac{\partial \chi^2}{\partial \vec{\xi}} = \left( \frac{\partial \vec{f}}{\partial \vec{\xi}} \right)^{\top} \vec{\lambda} \quad (2.4)$$

To find an extremum, we set these each to  $\vec{0}$  and solve. At GlueX, the KinFit uses the Newton-Raphson method. First, we Taylor expand the constraint equations to first order,

$$\vec{f}(\vec{\eta}, \vec{\xi}) \approx \vec{f}(\vec{\eta}_0, \vec{\xi}_0) + \left( \frac{\partial \vec{f}}{\partial \vec{\eta}} \right) \Big|_{\vec{\eta}_0, \vec{\xi}_0} (\vec{\eta} - \vec{\eta}_0) + \left( \frac{\partial \vec{f}}{\partial \vec{\xi}} \right) \Big|_{\vec{\eta}_0, \vec{\xi}_0} (\vec{\xi} - \vec{\xi}_0) \quad (2.5)$$

Assuming  $\vec{\eta}_0$  and  $\vec{\xi}_0$  are near the true minimum, we can set up an iterative method of approach,

$$\vec{f}_i + \left( \frac{\partial \vec{f}}{\partial \vec{\eta}} \right)_i (\vec{\eta}_{i+1} - \vec{\eta}_i) + \left( \frac{\partial \vec{f}}{\partial \vec{\xi}} \right)_i (\vec{\xi}_{i+1} - \vec{\xi}_i) = \vec{0} \quad (2.6)$$

where  $\vec{f}_i \equiv \vec{f}(\vec{\eta}_i, \vec{\xi}_i)$ ,  $\left( \frac{\partial \vec{f}}{\partial \vec{\eta}} \right)_i \equiv \left( \frac{\partial \vec{f}}{\partial \vec{\eta}} \right) \Big|_{\vec{\eta}_i, \vec{\xi}_i}$ , and  $\left( \frac{\partial \vec{f}}{\partial \vec{\xi}} \right)_i \equiv \left( \frac{\partial \vec{f}}{\partial \vec{\xi}} \right) \Big|_{\vec{\eta}_i, \vec{\xi}_i}$ . To carry out an iteration, we need to determine the next step in each of the free directions  $\vec{\eta}_{i+1}$  and  $\vec{\xi}_{i+1}$ . We start by writing the iterative forms of Equations (2.2) and (2.4) as

$$\mathbf{V}_{\vec{y}}^{-1}(\vec{\eta}_{i+1} - \vec{y}) + \left( \frac{\partial \vec{f}}{\partial \vec{\eta}} \right)_i^{\top} \vec{\lambda}_{i+1} = 0 \quad (2.7)$$

$$\left( \frac{\partial \vec{f}}{\partial \vec{\xi}} \right)_i^{\top} \vec{\lambda}_{i+1} = 0 \quad (2.8)$$

To obtain the next iterative estimate of  $\vec{\eta}$  by rearranging Equation (2.7) as

$$\vec{\eta}_{i+1} = \vec{y} - \mathbf{V}_{\vec{y}} \left( \frac{\partial \vec{f}}{\partial \vec{\eta}} \right)_i^{\top} \vec{\lambda}_{i+1} \quad (2.9)$$

Inserting this back into Equation (2.6), we get

$$\begin{aligned}
\vec{0} &= \underbrace{\vec{f}_i + \left( \frac{\partial \vec{f}}{\partial \vec{\eta}} \right)_i (\vec{y} - \vec{\eta}_i)}_{\vec{r}_i} - \underbrace{\left( \left( \frac{\partial \vec{f}}{\partial \vec{\eta}} \right)_i \mathbf{V}_{\vec{y}} \left( \frac{\partial \vec{f}}{\partial \vec{\eta}} \right)_i^\top \right)}_{\mathbf{S}_i} \vec{\lambda}_{i+1} + \left( \frac{\partial \vec{f}}{\partial \vec{\xi}} \right)_i (\vec{\xi}_{i+1} - \vec{\xi}_i) \\
\vec{0} &= \vec{r}_i - \mathbf{S}_i \vec{\lambda}_{i+1} + \left( \frac{\partial \vec{f}}{\partial \vec{\xi}} \right)_i (\vec{\xi}_{i+1} - \vec{\xi}_i) \\
\vec{\lambda}_{i+1} &= \mathbf{S}_i^{-1} \left( \vec{r}_i + \left( \frac{\partial \vec{f}}{\partial \vec{\xi}} \right)_i (\vec{\xi}_{i+1} - \vec{\xi}_i) \right)
\end{aligned} \tag{2.10}$$

We can plug this definition of  $\vec{\lambda}_{i+1}$  into Equation (2.8) to find the iterative update for  $\vec{\xi}$ :

$$\begin{aligned}
\vec{0} &= \left( \frac{\partial \vec{f}}{\partial \vec{\xi}} \right)_i^\top \mathbf{S}_i^{-1} \vec{r}_i + \underbrace{\left( \frac{\partial \vec{f}}{\partial \vec{\xi}} \right)_i^\top \mathbf{S}_i^{-1} \left( \frac{\partial \vec{f}}{\partial \vec{\xi}} \right)_i}_{\mathbf{U}_i} (\vec{\xi}_{i+1} - \vec{\xi}_i) \\
\vec{\xi}_{i+1} &= \vec{\xi}_i - \mathbf{U}_i^{-1} \left( \frac{\partial \vec{f}}{\partial \vec{\xi}} \right)_i^\top \mathbf{S}_i^{-1} \vec{r}_i
\end{aligned} \tag{2.11}$$

To perform the kinematic fit, we use the available measured observables and their covariances (contained in  $\vec{r}$ ,  $\mathbf{S}$ , and  $\mathbf{U}$ ) to update our estimate of  $\vec{\xi}$  via Equation (2.11). Next, we use that result to update  $\vec{\lambda}$  via Equation (2.10). Finally, we update  $\vec{\eta}$  via Equation (2.9). This process is repeated until the desired precision of these variables is met, and is guaranteed to converge as long as the initial values start near the minimum. The  $\chi^2$  value obtained from evaluating Equation (2.1) on the converged values tells us the quality of the fit. See Figure 2.4 for the distribution of  $\chi_v^2 \equiv \chi^2/\nu$ , where  $\nu$  is the number of degrees of freedom in the fit ( $\nu = 11$  for this analysis), for both the real data and Monte Carlo simulation of the signal.

The constraints  $\vec{f}$  used in this channel include four-momentum conservation,

$$\sum_{f \in \text{final}} p_f^\mu - \sum_{i \in \text{initial}} p_i^\mu = 0^\mu \tag{2.12}$$

where the sum over four-momenta of the initial-state particles must match that of the final-state particles, and the masses of each intermediate  $K_S^0$ ,

$$p_{K_S^0}^2 - m_{K_S^0}^2 = 0 \tag{2.13}$$

where  $m_{K_S^0}$  is the known mass of the  $K_S^0$  and  $p_{K_S^0}$  is the fitted estimate of the four-momentum reconstructed from the  $\pi^+ \pi^-$  four-momentum measured by the detectors. Additionally we constrain the initial and final positional vertices of each production step in the topology. For this channel, this means we constrain the initial production vertex and the point of closest approach of the  $K_S^0$ s and recoil proton, as well as the decay vertex of each  $K_S^0$  with

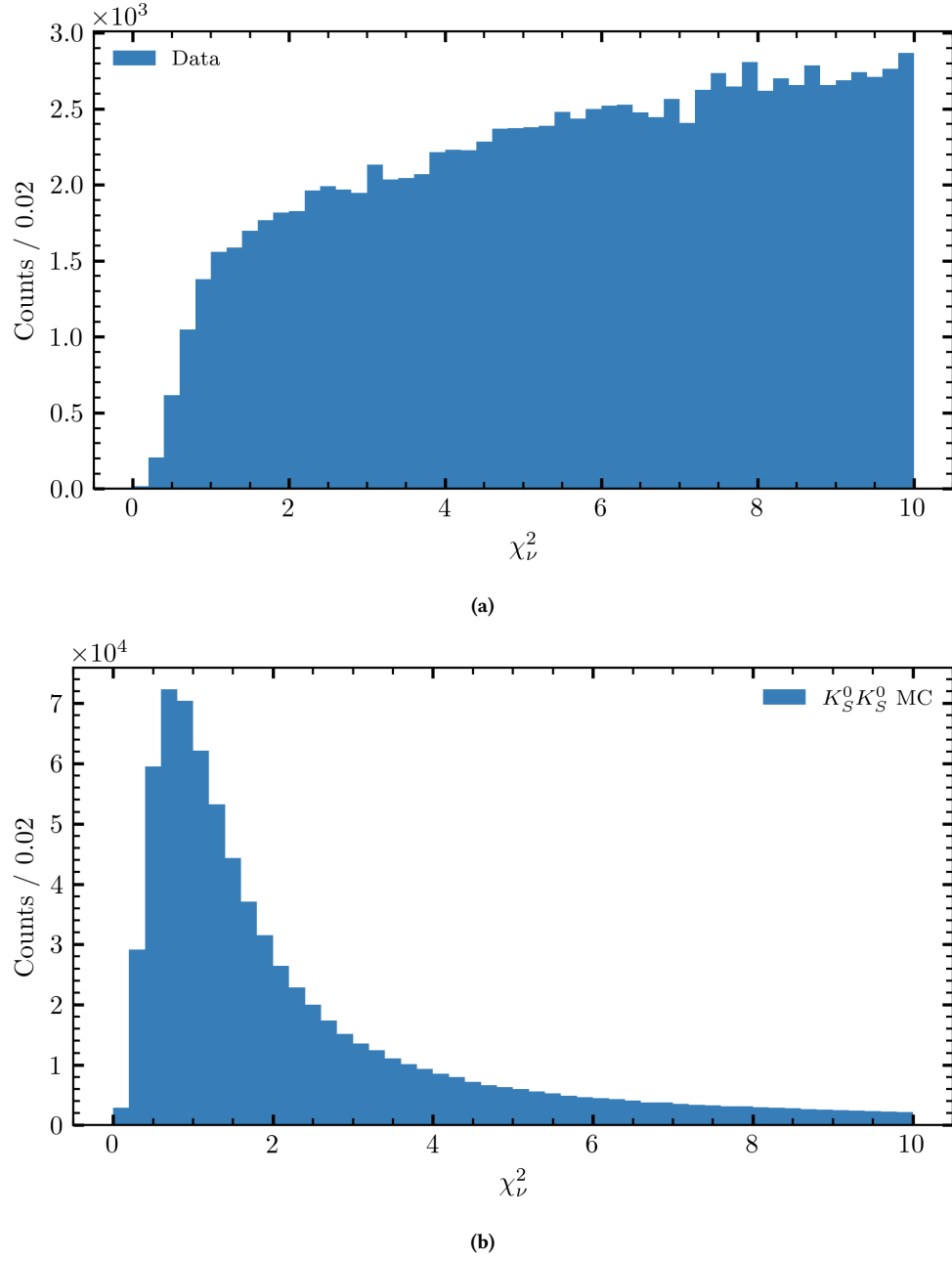


**Figure 2.4:** Distributions of  $\chi^2_v$  (the  $\chi^2$  per degree of freedom of the GlueX kinematic fit) for (a) data and (b) signal Monte Carlo after reconstruction cuts but before any fiducial selections from [Section 2.2](#). Note that the data extends past  $\chi^2_v > 10$ , but the plot was truncated for legibility. Both datasets have had accidental subtraction applied and combos flattened (see [Sections 2.1](#) and [2.2](#)).

the closest approach of its constituent pions. It is important to note that this vertex constraint cannot be done in the case where a  $K_S^0$  decays to  $2\pi^0$ , since the neutral pions will decay to  $2\gamma$  which can only be detected without tracking in the calorimeters. Because there is not a second point of detection for these photons, their trajectory and therefore the point at which the original  $\pi^0$  decayed is unknown, so there is no way to further reconstruct the kaon decay vertex because the point of closest approach is unknown<sup>7</sup>. Therefore, when we specify channels where one or both kaons decay as  $K_S^0 \rightarrow 2\pi^0$ , we do not include these  $K_S^0$ s in the kinematic fit at all, and must infer them by adding the  $\pi^0$  four-momenta (see [SECTION](#)). For the main  $\gamma p \rightarrow K_S^0 K_S^0 p \rightarrow 2\pi^+ 2\pi^- p$  channel, we have four constraints from four-momentum conservation, two mass constraints (one for each kaon), 14 vertex constraints (two for each constrained particle<sup>8</sup>, viz. four pions, two kaons, and a proton), and nine unknowns from the vertex constraints (the position of the vertex introduces three unknowns for each vertex, and there are three constrained vertices, viz. two kaon decays and the initial production vertex). This gives a total of 20 constraints with nine unknowns, or 11 degrees of freedom in the fit.

### Combos

While the initial interaction vertex in theory contains a single photon, in practice, the incident beam contains multiple tagged photons, any of which might provide the requisite energy needed to kinematically generate a given set of final-state tracks. Additionally, there could be multiple ways to recombine or identify final-state particles to arrive at the same event topology. The GlueX reconstruction process considers all valid combinations of tagged photons and sets of reconstructed final-state particles and saves each one in a sub-event called a “combo”. Each event has at least one of these combos, and some events may have many due to there being many candidate beam photons with similar energies. Since only one combo can be the true event, we need to flatten the data in a way that avoids double counting events. The method for doing so is discussed in [SECTION](#).

## 2.2 Data Selection for the $K_S K_S$ Channel

### Fiducial Cuts

### 2.3 sPlot Weighting

At this stage in the analysis, we have no more simple cuts which can improve the signal-to-background ratio in the dataset, but we know there must still be background remaining, as is indicated by the excess events with small kaon

<sup>7</sup>The best we could do would be to assume the kaon decayed at the initial reaction vertex inside the target, which is not only unrealistic given that kaons decay via the weak interaction, but also causes problems later when we try to calculate the kaon lifetime to use in event weighting in [Section 2.3](#).

<sup>8</sup>This is because we independently constrain the distance of a particle to the unknown vertex along two planes, the “bend” plane and the “non-bend” plane, named for being equal/perpendicular to the plane in which the trajectory of the particle is bending due to the magnetic field at the vertex point.

rest-frame lifetimes seen in [Figure 2.5](#). In this figure, we see that one of the intrinsic properties of a  $K_S^0$ , its well-known lifetime, is not distinct in the data. Rather, we seem to have at least two exponential slopes in the rest-frame lifetime distribution of each kaon, one which is close to what we see in signal Monte Carlo, and another which is similar to the  $4\pi$  background Monte Carlo. We must now turn to more elaborate methods of separating the signal from this potential background seepage. The primary method we will use to do this is sPlot[47]<sup>9</sup>, a weighting scheme which corrects the naïve probabilistic weights one might first think to construct (dubbed “inPlot”). We begin by giving a basic explanation of inPlot before describing the sPlot correction.

For all of the statistical weighting methods which will be mentioned here, we need some model for the signal and background probability distribution functions (PDFs) for some “discriminating” variable. This variable is called “discriminating” because it is the variable for which we know the shape of these distributions beforehand. The usual example is a “bump-on-a-background”, in which the discriminating variable may be a mass distribution ( $m$ ) where signal events show up as a peaking structure while background events are more uniformly distributed. In such situations, it is common to use the extremes of the mass distribution (sidebands) as estimates of the background everywhere, weighting these events negatively while the events in the peak are weighted positively (a sideband subtraction). Rather than specifying peak and sideband regions, we can fit the mass distribution to some mixture of a signal (peak) PDF  $f_S(m)$  and a background (flat) PDF  $f_B(m)$ . From such a fit, we obtain estimated number of signal ( $N_S$ ) and background ( $N_B$ ) events in our dataset (and possibly some shape parameters for the signal and background PDFs). We could then assign weights to each event as in [Equation \(2.14\)](#),

$$w(m) = \frac{N_S f_S(m)}{N_S f_S(m) + N_B f_B(m)} \quad (2.14)$$

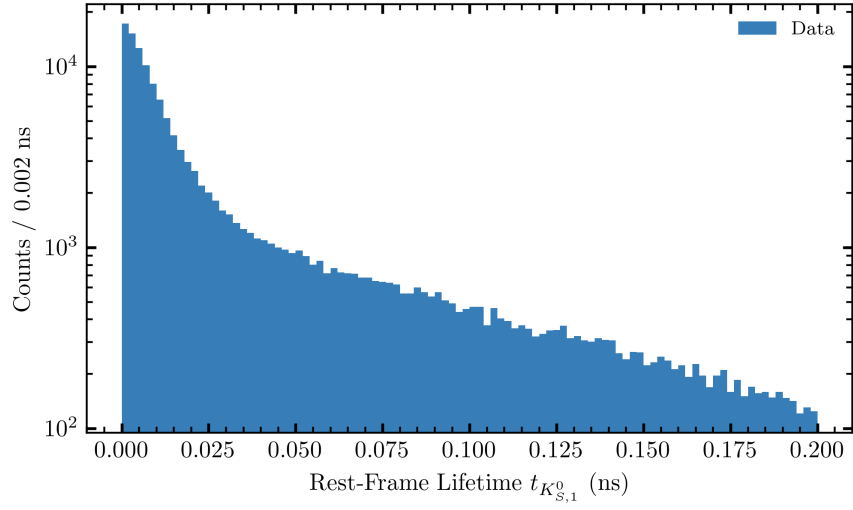
We might want to look at the “signal” inPlots for the decay angles  $\theta$  and  $\phi$  (control variables) in the helicity system after calculating the inPlot weights from a fit to the mass distribution (discriminating variable). However, as shown by Pivk and Le Diberder[47], we can only use inPlot in cases where the control variables are totally correlated with the discriminating variable<sup>10</sup>  $y$ . In other words, our example would only be valid if  $\theta = \theta(m)$  and  $\phi = \phi(m)$ . For the time being, let us assume that this is not the case, and that we wish to use the distribution of some variable which is totally uncorrelated with the variables we are plotting and analyzing<sup>11</sup>. A correction term can be applied to give us the sPlot version of [Equation \(2.14\)](#),

$$w(y) = \tilde{w}(y) \frac{V_{SS} f_S(y) + V_{SB} f_B(y)}{N_S f_S(y) + N_B f_B(y)}, \quad \text{where } V_{ij}^{-1} = \sum_y \frac{\tilde{w}(y) f_i(y) f_j(y)}{(N_S f_S(y) + N_B f_B(y))^2} \quad (2.15)$$

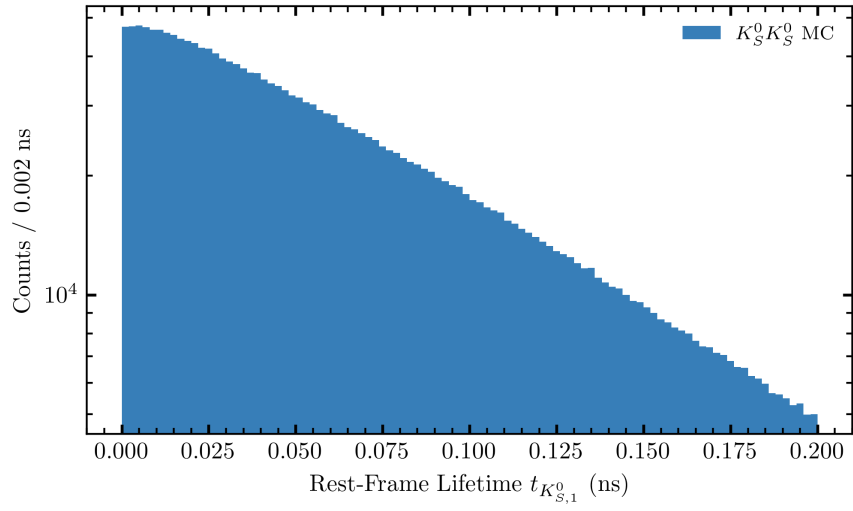
<sup>9</sup>This is stylized as *sPlot* in the original paper, but I find this tedious to type and to read.

<sup>10</sup>In practice, more than one discriminating variable can be used.

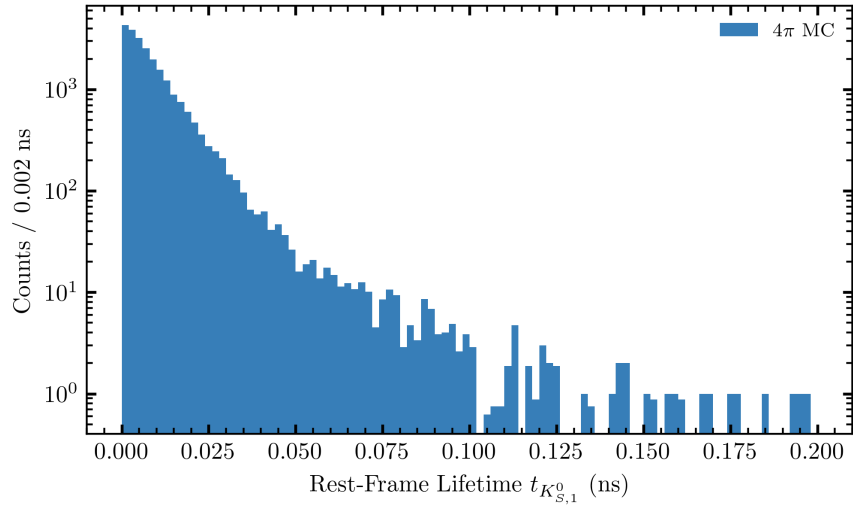
<sup>11</sup>Total (un)correlation is a very strict requirement, but we will later see that small modifications to the sPlot method can permit amounts of correlation between the two extremes.



(a)



(b)



(c)

**Figure 2.5:** The rest-frame lifetime of kaons in (a) data, (b) signal Monte Carlo, and (c) background Monte Carlo. The data distribution clearly contains two exponential slopes: a peak which resembles the  $4\pi$  Monte Carlo distribution, and a tail of true  $K_S^0$ s which resembles the signal Monte Carlo.

where  $y$  represents any set of discriminating variables (not necessarily a mass), and  $\tilde{w}(y)$  is any pre-existing weight associated with the event (weights from accidental subtraction, for instance). The  $V^{-1}$  matrix can also be understood as the covariance matrix between the free parameters  $N_S$  and  $N_B$  in the fit of the signal-background mixture,  $V_{ij}^{-1} = -N \frac{\partial^2 \ln \mathcal{L}}{\partial N_i \partial N_j}$ , although there is reason to believe that direct calculation by inverting the Hessian matrix from the fit will lead to less accurate results than the manual calculation method given in Equation (2.15)[48].

Now that we have a method of assigning weights, we must pick the discriminating variables. As mentioned, these weighting methods work well on the classic “bump-on-a-background” distributions because it is easy to identify the signal and background PDFs, but because the mass of the kaons is constrained in the kinematic fit, the fitted mass of each kaon is just a  $\delta$ -function and combination of measured masses for each  $\pi^+\pi^-$  pair will yield a Normal distribution with little to no apparent background (by construction), so we must be a bit more clever in selecting discriminating variables. By examining the BGEN analysis done in [TODO: PREVIOUS SECTION], we can see that most likely sources of background arise when the intermediate kaons are absent from the reaction:  $\gamma p \rightarrow 4\pi p$ . This reaction has the  $K_S K_S$  final state, so pairs of pions which reconstruct close enough to kaons will be almost indistinguishable in the data. However, they differ in one key way, namely that the  $K_S$  intermediate contains a strange quark while the  $\pi^+\pi^-$  decay state does not, so such a decay must occur via the weak interaction, which is notably slower than the strong interaction which would produce pion pairs with no intermediate kaon. In other words, while the signal’s rest-frame lifetime distribution should have an exponential slope near the  $K_S$  lifetime, the background would theoretically have nearly zero rest-frame lifetime for every event, or a much smaller exponential slope in practice<sup>12</sup>.

Therefore, we will begin by generating both a signal and background dataset in Monte Carlo. We then interpret both datasets as if they were our desired channel by running them through the GlueX reconstruction and reaction filter, as well as all of our selections up to this point. We can then fit the rest-frame lifetime of each dataset to an exponential model,

$$f(t; \lambda) = \lambda \exp\{-\lambda t\}, \quad (2.16)$$

where  $\lambda \equiv 1/\tau$ , the lifetime of the kaon in question. Since we have two independently decaying kaons, we should really form a joint distribution for both, where we will assume each kaon has the same average lifetime:

$$f(t_1, t_2; \lambda) = \lambda^2 \exp\{-\lambda t_1\} \exp\{-\lambda t_2\} \quad (2.17)$$

Both the signal and background distributions can be modeled in this way, giving us only two free parameters,  $\lambda_S$  and  $\lambda_B$  for the signal and background respectively, to fit.

---

<sup>12</sup>An exponential distribution is just what best fits the rest-frame lifetime distribution in the  $4\pi$  Monte Carlo and has no physical implication.

We can then use a mixture of exponential distributions with both signal and background slopes to fit the entire dataset:

$$f(t_1, t_2; z, \lambda_S, \lambda_B) \equiv z f(t_1, t_2; \lambda_S) + (1 - z) f(t_1, t_2; \lambda_B) \quad (2.18)$$

where  $z$  is the signal fraction of the total number of events  $N$ . From its fit value, we can determine values of  $N_S = z \cdot N$  and  $N_B = (1 - z) \cdot N$  to use in Equation (2.15) and complete the weighting procedure. We can perform this fit by minimizing the negative log-likelihood function,

$$-2 \ln \mathcal{L}(z, \lambda_S, \lambda_B) = -2 \sum_i^N \tilde{w}_i \ln f(t_{1,i}, t_{2,i}; z, \lambda_S, \lambda_B) \quad (2.19)$$

where again, we include any pre-existing weights  $\tilde{w}$  in the fit.

### Non-Factorizing sPlot

Over the course of the previous discussion, it was assumed that the discriminating variables,  $t_1$  and  $t_2$ , were statistically independent from the control variables we wish to use in later analyses. The set of control variables must include all variables we use as inputs to the partial-wave analysis in Chapter 3, including the invariant mass  $m$  of the  $K_S^0 K_S^0$  system and the helicity angles  $\theta$  and  $\varphi$  of the decay. We should now confirm that the rest-frame lifetimes are totally uncorrelated with these control variables (in other words, show that they are statistically independent). To test for statistical independence between  $t_{1,2}$  and a given control variable, we first split our dataset into  $M$  evenly-spaced quantiles in that control variable, which ensures each bin gets roughly the same number of events. Next, we calculate the likelihood of a null hypothesis which assumes the variables are statistically independent by fitting all datasets simultaneously with shared  $\lambda_S$  and  $\lambda_B$  parameters. We then calculate the likelihood of an alternative hypothesis, which assumes statistical dependence, by finding the joint likelihood of independent fits of  $\lambda_S$  and  $\lambda_B$  over each quantile. The result of these fits can be formulated as a likelihood ratio,

$$\Lambda = -2 \ln \frac{\sup \mathcal{L}_{H_0}}{\sup \mathcal{L}_{H_1}} = -2 \ln \frac{\sup \prod_i^M \mathcal{L}_i(z_i, \lambda_S, \lambda_B)}{\sup \prod_i^M \mathcal{L}_i(z_i, \lambda_{S,i}, \lambda_{B,i})} \quad (2.20)$$

where  $\mathcal{L}_{H_0}$  and  $\mathcal{L}_{H_1}$  are the likelihoods of the null and alternative hypotheses respectively, the supremum indicates we are maximizing these likelihoods (in a maximum likelihood fit), the product  $\prod_i^M$  iterates over each quantile of data in the given control variable, and  $\mathcal{L}_i$  is the likelihood evaluated over data in the  $i$ th quantile.  $\Lambda$  is  $\chi^2$  distributed with  $2M - 2$  degrees of freedom (the difference between  $M + 2$  free parameters in the null hypothesis, a signal fraction  $z_i$  for each quantile plus the two exponential slopes shared across all quantiles, and  $3M$  in the alternative hypothesis, a signal fraction and two exponential slopes for each quantile). The factor of 2 is required because  $\ln \mathcal{L}(\theta_1, \dots, \theta_i) \sim -\frac{1}{2} \chi_i^2$  asymptotically with sample size, according to Wilks' theorem. We can obtain a  $p$ -value representing the likelihood of the null hypothesis being true by evaluating the  $p$ -value:



$$p = 1 - F_{\chi^2_{2M-2}}(\Lambda) \quad (2.21)$$

where  $F_{\chi^2_{2M-2}}(\Lambda)$  is the cumulative distribution function of a  $\chi^2$  distribution with  $2M - 2$  degrees of freedom. Following this procedure for the invariant mass of  $K_S^0 K_S^0$ <sup>13</sup>, the  $p$ -values for each number of quantiles can be seen in the first row of [Table 2.3](#) and in [Figure 2.6](#), which depicts the case with four quantiles. The calculated  $p$ -values tend to be very small, implying that we should reject the null hypothesis and accept that the discriminating (rest-frame lifetime) and control (invariant mass of  $K_S^0 K_S^0$ ) variables are not statistically independent. This means we cannot use a traditional sPlot to weight our data.

Fortunately, the process for obtaining the correct weights is straightforward, we simply allow for more than one signal and background component in the fit and sum over all signal components when we calculate the final weight values [48]. Since the weights corresponding to each signal component in the sPlot can be added to each other to obtain a joint weight [47], [Equation \(2.15\)](#) can be extended to allow multiple signal and background components:

$$w(x) = \frac{\sum_j V_{S_0j} f_j(x)}{\sum_k N_k f_k(x)} + \dots + \frac{\sum_j V_{S_nj} f_j(x)}{\sum_k N_k f_k(x)}, \quad \text{where } V_{ij}^{-1} = \sum_x \frac{f_i(x) f_j(x)}{(\sum_k N_k f_k(x))^2} \quad (2.22)$$

and  $S_i$  are the indices of the signal components.

We can further verify the need for non-factorizing sPlot by performing the factorization test described in [Equations \(2.20\) and \(2.21\)](#) to the signal and background Monte Carlo, with a slight modification to the number of free parameters, since we only need to fit either a signal or background component rather than a mixture:

$$p = 1 - F_{\chi^2_{M-1}} \quad \text{where } \Lambda = -2 \ln \frac{\sup \prod_i^M \mathcal{L}_i(\lambda)}{\sup \prod_i^M \mathcal{L}_i(\lambda_i)} \quad (2.23)$$

The results of these tests over the signal and background Monte Carlo can also be found in the last two rows of [Table 2.3](#) and are visualized for four quantiles in [Figure 2.7](#). Again, the significantly small  $p$ -values justify the use of non-factorizing sPlot across both the signal and background components, meaning that we need at least two signal and two background components in the final sPlot weighting.

### Application of Weights

The only thing left to do is determine how many signal and background components we should use in the weighting procedure. To this end, we now turn to the Monte Carlo simulations of the signal and  $4\pi$ -background. By choosing a number of quantiles in invariant mass corresponding to the number of components, we can fit single exponential distributions to each quantile in the simulated signal and background. For instance, if we chose to use two signal components and three background components, we would divide the signal Monte Carlo into two quantiles and the

<sup>13</sup>No significant statistical dependence was found for the helicity angles.

| Data Type        | # quantiles               |                           |                           |
|------------------|---------------------------|---------------------------|---------------------------|
|                  | 2<br>$p$                  | 3<br>$p$                  | 4<br>$p$                  |
| Data             | $1.26 \times 10^{-101}$   | $9.94 \times 10^{-103}$   | $4.49 \times 10^{-112}$   |
| $K_S^0 K_S^0$ MC | $< 2.23 \times 10^{-308}$ | $< 2.23 \times 10^{-308}$ | $< 2.23 \times 10^{-308}$ |
| $4\pi$ MC        | $1.87 \times 10^{-05}$    | $1.00 \times 10^{-04}$    | $7.38 \times 10^{-05}$    |

**Table 2.3:** The probability of accepting the null hypothesis (that the rest-frame lifetime is statistically independent of the invariant mass of  $K_S^0 K_S^0$ ) for the tests described in Equation (2.20) for data and Equation (2.23) for Monte Carlo with the given number of quantiles. All values are calculated with a  $\chi^2_v < 3.0$  selection on each type of data over all run period combined. Values listed as  $< 2.23 \times 10^{-308}$  are nonzero but smaller than the smallest representable 64-bit floating point number

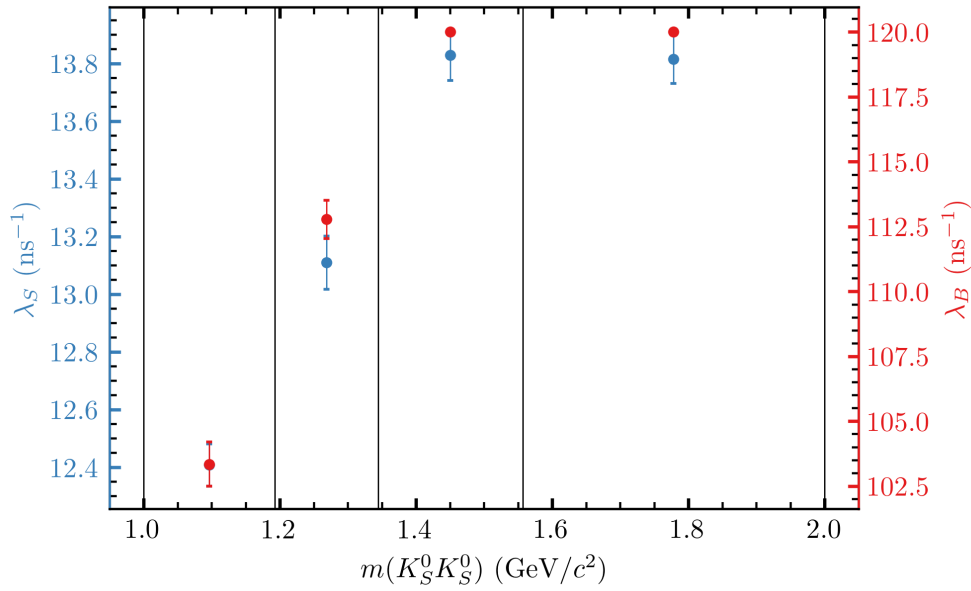


**Figure 2.6:** Exponential slopes from fits over four quantiles in  $m(K_S^0 K_S^0)$  (x-axis) to a mixture of signal (left y-axis) and background (right y-axis) components. These fits show a definite statistical dependence between rest-frame lifetime and the invariant mass of  $K_S^0 K_S^0$ , as described in Table 2.3. All values are calculated with a KinFit  $\chi^2_v < 3.0$  selection on each type of data over each run period.

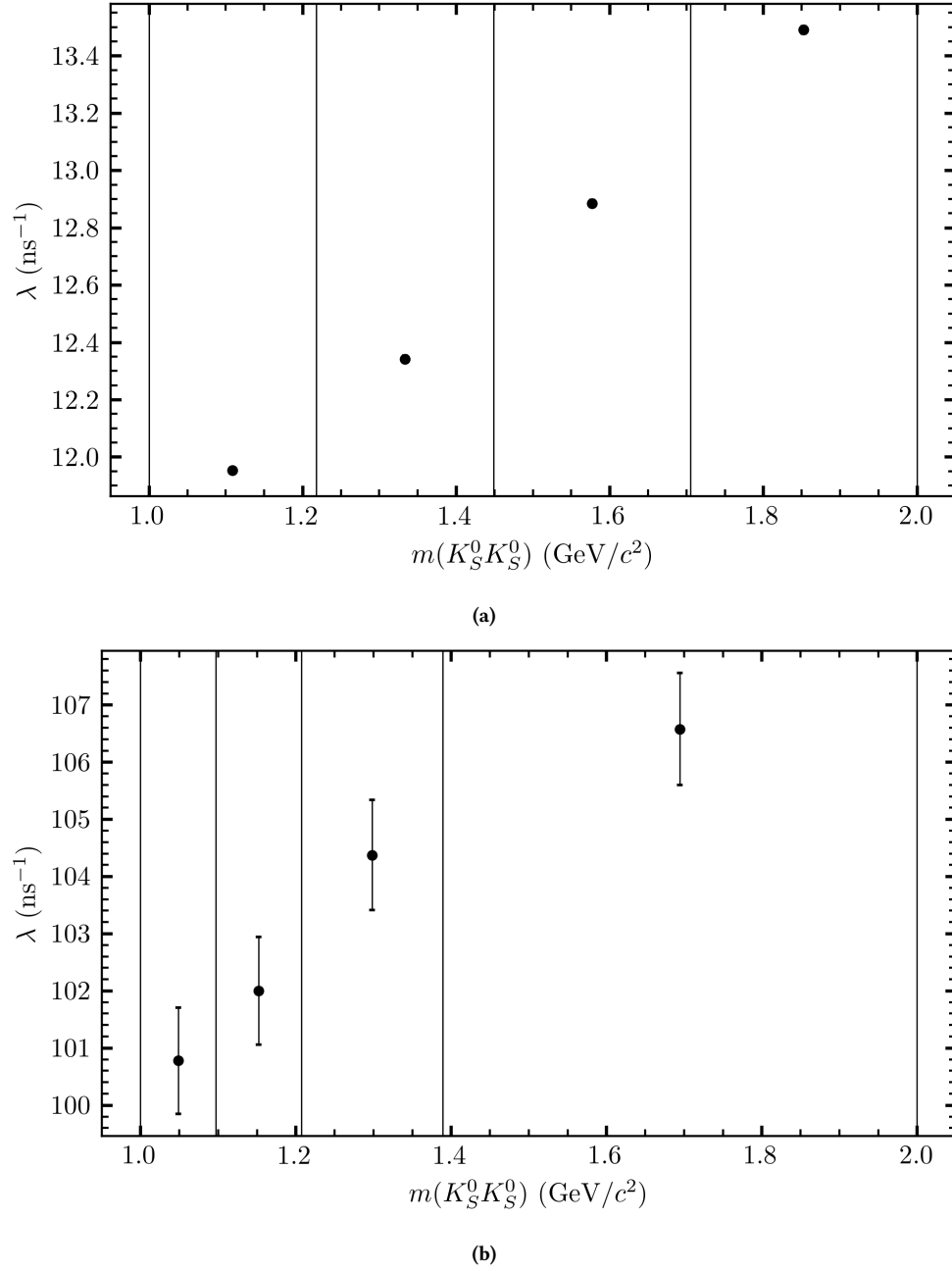


**Figure 2.7:** Exponential slopes from fits over four quantiles in  $m(K_S^0 K_S^0)$  ( $x$ -axis) of the (a) signal and (b) background Monte Carlo rest-frame lifetime distributions. Both show a definite statistical dependence between rest-frame lifetime and the invariant mass of  $K_S^0 K_S^0$ , as described in Table 2.3. All values are calculated with a KinFit  $\chi^2 < 3.0$  selection on each type of data over each run period.

background Monte Carlo into three, and fit each quantile to an exponential distribution to obtain a set of two  $\lambda_S$  and three  $\lambda_B$  values. The resulting  $\lambda_S$  and  $\lambda_B$  values could then be used as a starting point for a multi-component fit to the data. Alternatively, both the signal and background or just the signal could be fixed to the values from the fits to simulations, and only the yields (or the yields and background  $\lambda$ s) would be allowed to float in the fit to data. We will refer to the first case, where the fit parameters from Monte Carlo are free, as *A*, the case where the signal  $\lambda$ s are fixed as *B*, and the case where all  $\lambda$ s are fixed (and the only floating parameters are the yields of each component) as *C*. To select a model, we can use the relative Akaike Information Criterion (AIC) [49] and Bayesian Information Criterion (BIC) [50]:

$$rAIC \equiv AIC - AIC_{\min} \quad \text{where } AIC \equiv 2k - 2 \ln \mathcal{L} \quad (2.24)$$

$$rBIC \equiv BIC - BIC_{\min} \quad \text{where } BIC \equiv k \ln N - 2 \ln \mathcal{L} \quad (2.25)$$

$$(2.26)$$

where  $k$  is the number of free parameters and  $N$  is the number of events in the dataset. The optimal model will minimize these criteria. In [Table 2.4](#), all of the relative AIC and BIC values are shown. Excluding cases with only one signal or background component (restricting to models which have non-factorizing signal and background components), the minimizing values for most run periods tend to use two or three signal and two background components, and they both use method *B*, where the signal components are fixed to values obtained from Monte Carlo while the background components are initialized at Monte Carlo values but allowed to float in the fit. We will use the minimal non-factorizing model, method *B* with two signal and two background components, denoted  $B(2, 2)$ , as our weighting method. See [Figure 2.8](#) for the result of this fit. The selection of method *B* is also interesting as it could describe a case where another background which is not modeled in the background Monte Carlo is present and has a similar exponential slope. Since these slopes are free in the fit to the data, they may anticipate this unknown slope better than the fixed case (method *C*), and method *B* also explicitly assumes the Monte Carlo for true signal kaons is correct and fixes their component slopes (unlike method *A*).

| Method   | # Components |            | $rAIC$       | $rBIC$       |
|----------|--------------|------------|--------------|--------------|
|          | Signal       | Background |              |              |
| <i>A</i> | 1            | 1          | <u>0.000</u> | <u>0.000</u> |
|          | 1            | 2          | 4.000        | 25.420       |
|          | 1            | 3          | 8.004        | 50.843       |
|          | 2            | 1          | 4.000        | 25.420       |
|          | 2            | 2          | 8.000        | 50.839       |
|          | 2            | 3          | 12.003       | 76.261       |
|          | 3            | 1          | 8.000        | 50.839       |
|          | 3            | 2          | 12.002       | 76.261       |
|          | 3            | 3          | 16.002       | 101.681      |
| <i>B</i> | 1            | 1          | 312.365      | 301.655      |
|          | 1            | 2          | 213.928      | 224.638      |
|          | 1            | 3          | 217.324      | 249.453      |
|          | 2            | 1          | 23.929       | 23.929       |
|          | 2            | 2          | 9.758        | 31.177       |
|          | 2            | 3          | 13.629       | 56.468       |
|          | 3            | 1          | 2.001        | 12.711       |
|          | 3            | 2          | 6.004        | 38.134       |
|          | 3            | 3          | 10.002       | 63.551       |
| <i>C</i> | 1            | 1          | 1695.033     | 1673.614     |
|          | 1            | 2          | 1305.143     | 1294.433     |
|          | 1            | 3          | 1197.528     | 1197.528     |
|          | 2            | 1          | 1661.600     | 1650.890     |
|          | 2            | 2          | 1245.238     | 1245.238     |
|          | 2            | 3          | 1128.344     | 1139.053     |
|          | 3            | 1          | 1661.070     | 1661.070     |
|          | 3            | 2          | 1247.365     | 1258.074     |
|          | 3            | 3          | 1131.169     | 1152.588     |

**Table 2.4:** Relative AIC and BIC values for each fitting method. The absolute minimum values in each column are underlined, and the minimums excluding models with only one signal or background component are boxed.

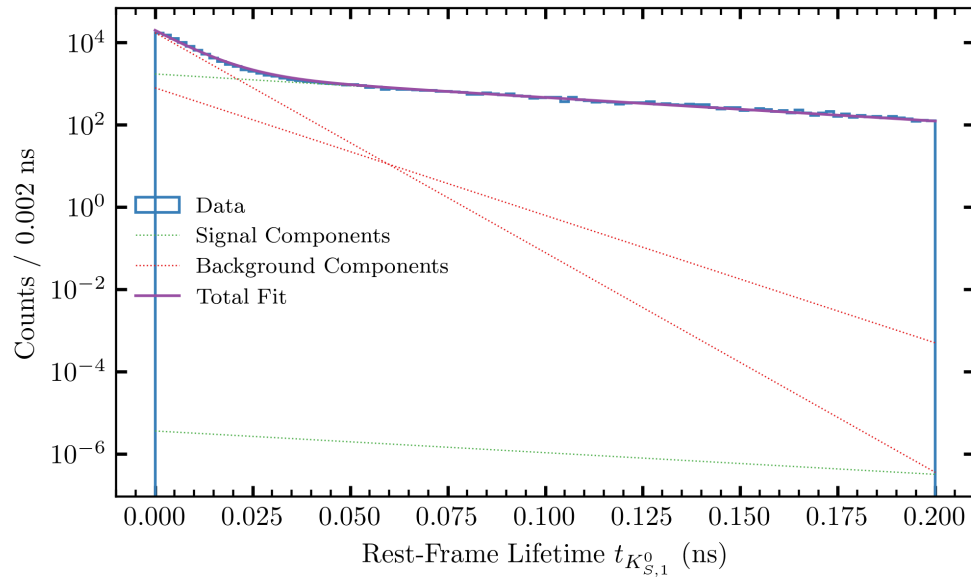


**Figure 2.8:** Fit of Equation (2.18) to data using method  $B(2, 2)$ . True kaon events are prominent in the tail of the distribution, whereas background events peak strongly near zero. All values are calculated with a  $\text{KinFit } \chi^2_v < 3.0$  selection on each type of data over each run period. The second signal component tends to be very small but non-zero across all datasets.

## Chapter 3

# Partial-Wave Analysis

### 3.1 Amplitude Formalism

TODO: cite <http://scipp.ucsc.edu/~haber/ph218/ExperimentersGuideToTheHelicityFormalism.pdf> and S.U. Chung spin formalisms

Now we embark on the topic of amplitudes. We wish to describe the dynamics of our reaction in a way that allows us to extract quantum numbers like spin from our data. There are several difficulties in doing so: First, we are trying to determine the properties of many particles at once, and we know that many resonances in this channel overlap in mass space. This precludes the use of a simple Breit-Wigner description of most of these resonances, as overlapping Breit-Wigners do not preserve unitarity. Second, the GlueX experiment uses a linearly polarized photon beam, so it behooves us to use a formalism which can include this polarization. Finally, there are many resonances in this channel, and while we have the largest photoproduction dataset to date, we are still relatively data limited, which further complicates any dynamical description.

#### Single-Particle Helicity States

We begin by defining a set of observables which are independent of frames and rotations on those frames. This is known as the helicity formalism, where helicity resembles the spin projection along the axis of a particle's motion. First, we define a rotation  $R(\alpha, \omega, \gamma)$  as a matrix whose action on a vector is a rotation about the Euler angles  $\alpha$ ,  $\omega$ , and  $\gamma$ . For each rotation, we can define a unitary operator  $U[R]$  which has the group property  $U[R_2 R_1] = U[R_2] U[R_1]$  as it is an operator on the group  $SO(3)$ . Being an operator on  $SO(3)$ , we can also write it as

$$U[R(\alpha, \omega, \gamma)] = e^{-i\alpha J_z} e^{-i\omega J_y} e^{-i\gamma J_z} \quad (3.1)$$

We can then describe the matrix elements of this operator in the angular momentum eigenbasis  $|jm\rangle$  (representing a spin- $j$  particle where  $m$  is the projection of spin onto the  $\hat{z}$ -axis) with the Wigner D-matrix:

$$U[R(\alpha, \omega, \gamma)] \equiv \sum_{m'} |jm\rangle D_{m'm}^j(R(\alpha, \omega, \gamma)) \quad (3.2)$$

where

$$D_{m'm}^j(\alpha, \omega, \gamma) \equiv e^{-im'\alpha} d_{m'm}^j e^{-im\gamma} \quad (3.3)$$

and

$$d_{m'm}^j(\omega) = \langle jm' | e^{-i\omega J_y} | jm \rangle \quad (3.4)$$

We can further extend this eigenbasis to include linear momentum by introducing Lorentz boosts  $L(\vec{\beta})$ . We denote the operation of a boost along the  $\hat{z}$ -axis with velocity  $\beta$  as  $L_z(\beta)$ . A boost in any direction described by polar angles  $(\theta, \varphi)$  can be achieved by rotating the  $\hat{z}$ -axis to align with the direction vector, boosting in the new  $\hat{z}$ -direction, and rotating back:

$$L(\vec{\beta}) = R(\varphi, \theta, 0) L_z(\beta) R^{-1}(\varphi, \theta, 0) \quad (3.5)$$

Together, the space of rotations and boosts defines the Lorentz group, where each arbitrary Lorentz transformation  $\Lambda$  has a unitary operator  $U[\Lambda]$  with the group property  $U[\Lambda_2 \Lambda_1] = U[\Lambda_2] U[\Lambda_1]$ , so in terms of operators, we can also write

$$U[L(\vec{p})] = U[R(\varphi, \theta, 0)] U[L_z(p)] U^{-1}[R(\varphi, \theta, 0)] \quad (3.6)$$

Finally, this allows us to define the “canonical” basis for a single particle as

$$U[L(\vec{p})] |jm\rangle \equiv |\vec{p}, jm\rangle \quad (3.7)$$

Unfortunately, the quantum number  $m$  is only valid in the rest frame of the state because the  $\hat{z}$ -axis of the rest frame is not equivalent to the  $\hat{z}$ -axis in any arbitrarily Lorentz-transformed frame. Therefore, we will define helicity  $\lambda$  as the projection of spin along the direction of motion and introduce new helicity states,

$$|\vec{p}, j\lambda\rangle = U[L(\vec{p})] U[R(\varphi, \theta, 0)] |j\lambda\rangle = U[R(\varphi, \theta, 0)] U[L_z(p)] |j\lambda\rangle \quad (3.8)$$

In this definition, we have two ways of obtaining the helicity frame: We can either rotate the state first such that the quantization axis is aligned with  $\vec{p}$  and then boost in the  $\hat{p}$ -direction or we can first boost in the  $\hat{z}$ -direction and then rotate. In either equivalent case,  $\lambda$  is invariant under rotations as well as boosts parallel to  $\vec{p}$ . Finally, we can define these helicity states over a basis of canonical states:



$$|\vec{p}, j\lambda\rangle = \sum_m D_{m\lambda}^j(R(\varphi, \theta, 0)) |\vec{p}, jm\rangle \quad (3.9)$$

The single-particle states are normalized such that

$$\begin{aligned} \langle \vec{p}', j'\lambda' | \vec{p}, j\lambda \rangle &= \tilde{\delta}(\vec{p}' - \vec{p}) \delta_{j'j} \delta_{\lambda'\lambda} \\ \text{with } \tilde{\delta}(\vec{p}' - \vec{p}) &= (2\pi)^3 (2E) \delta^{(3)}(\vec{p}' - \vec{p}) \end{aligned} \quad (3.10)$$

since the Lorentz-invariant phase space element is given by  $\tilde{d}p = \frac{d^3\vec{p}}{(2\pi)^3(2E)}$ . This gives the following representation of the identity:

$$\sum_{j\lambda} \int |\vec{p}, j\lambda\rangle \tilde{d}p \langle \vec{p}, j\lambda| = I \quad (3.11)$$

### Two-Particle Helicity States

Of course, we would like to extend these states to be able to talk about interactions and decays. For notation, I will use  $\Omega$  to represent the polar angles  $\theta$  and  $\varphi$  and  $\emptyset$  to describe the specific value of 0 for both of these angles. Similarly,  $R_\Omega$  and  $R_\emptyset$  will represent the corresponding rotation operators (the second being a null rotation the direction of the  $\hat{z}$ -axis).  $R$  without subscript or angles will represent an arbitrary rotation whose angles are not important for the derivation.

Next, we can define a joint state of two particles with masses  $w_1$  and  $w_2$  (to avoid confusion with angular moments) and spins  $s_1$  and  $s_2$ . In the center-of-momentum (COM) frame, these particles are back-to-back, and we can define the momentum of particle 1 as  $\vec{p}$  with direction  $\Omega$  and particle 2 as  $-\vec{p}$ . Then the joint canonical state, up to a normalization constant  $\mathcal{N}$ , is given by

$$|\Omega, s_1 m_1 s_2 m_2\rangle = \mathcal{N} U[L(\vec{p})] |s_1 m_1\rangle U[L(-\vec{p})] |s_2 m_2\rangle \quad (3.12)$$

Such a state can also be described with a total spin  $s$  and moment  $m_s$ :

$$|\Omega, sm_s\rangle = \sum_{m_1 m_2} (s_1 m_1 s_2 m_2 | sm_s) |\Omega, s_1 m_1 s_2 m_2\rangle \quad (3.13)$$

Here,  $(s_1 m_1 s_2 m_2 | sm_s)$  is the Clebsch-Gordan coefficient describing the angular momentum coupling. Next, we can add additional angular momentum apart from the spin. For a system with angular momentum  $\ell$  with moment  $m$ , we use the fact that  $\langle \Omega | \ell m \rangle = Y_\ell^m(\Omega)$  (spherical harmonics) to define

$$|\ell m sm_s\rangle = \int d\Omega Y_\ell^m(\Omega) |\Omega; sm_s\rangle \quad (3.14)$$

Next, the spin  $s$  and angular momentum  $\ell$  can be coupled into the total angular momentum  $J$  with moment  $M$ :

$$|JM\ell m s\rangle = \sum_{m s} (\ell m s | JM) |\ell m s\rangle \quad (3.15)$$

This coupled state is still in the canonical formalism, and we would like to use the helicity basis. Using [Equation \(3.8\)](#),

$$|\Omega, s_1 \lambda_1 s_2 \lambda_2\rangle = \mathcal{N} U[R_\Omega] \underbrace{(U[L_z(p)] |s_1 \lambda_1\rangle U[L_{-z}(p)] |s_2, -\lambda_2\rangle)}_{|\emptyset, s_1 \lambda_1 s_2 \lambda_2\rangle} \quad (3.16)$$

To obtain states with a total angular momentum, we can integrate over the space of all rotations, weighted by Wigner D-matrices:

$$|JM s_1 \lambda_1 s_2 \lambda_2\rangle = \frac{N_J}{2\pi} \int dR D_{M\mu}^{J*}(R) U[R] |\emptyset, s_1 \lambda_1 s_2 \lambda_2\rangle \quad (3.17)$$

This is, of course, incomplete, as we have not defined the normalization factor  $N_J$  or the coupling  $\mu$  which relates helicities to total angular momentum. To do both, let us specify the rotation  $R$  as follows,

$$\begin{aligned} |JM s_1 \lambda_1 s_2 \lambda_2\rangle &= \frac{N_J}{2\pi} \int dR D_{M\mu}^{J*}(R) U[R(\varphi, \theta, \gamma)] |\emptyset, s_1 \lambda_1 s_2 \lambda_2\rangle \\ &= \frac{N_J}{2\pi} \int dR D_{M\mu}^{J*}(R) U[R(\varphi, \theta, 0)] U[R(0, 0, \gamma)] |\emptyset, s_1 \lambda_1 s_2 \lambda_2\rangle \\ &= \frac{N_J}{2\pi} \int dR D_{M\mu}^{J*}(R) e^{-i(\lambda_1 - \lambda_2)\gamma} U[R(\varphi, \theta, 0)] |\emptyset, s_1 \lambda_1 s_2 \lambda_2\rangle \\ &= \frac{N_J}{2\pi} \int d\Omega d\gamma e^{iM\varphi} d_{M\mu}^{J*} e^{i\mu\gamma} e^{-i(\lambda_1 - \lambda_2)\gamma} U[R(\varphi, \theta, 0)] |\emptyset, s_1 \lambda_1 s_2 \lambda_2\rangle \\ &= \frac{N_J}{2\pi} \int d\Omega d\gamma e^{iM\varphi} d_{M\mu}^{J*} e^{i(\mu - (\lambda_1 - \lambda_2))\gamma} |\Omega, s_1 \lambda_1 s_2 \lambda_2\rangle \\ &= N_J \int d\Omega D_{M\lambda}^{J*}(R_\Omega) |\Omega, s_1 \lambda_1 s_2 \lambda_2\rangle \end{aligned} \quad (3.18)$$

with  $\lambda = \lambda_1 - \lambda_2$

It can be shown that the normalization is  $\mathcal{N} = \frac{1}{4\pi} \sqrt{\frac{p}{s}}$  where  $p$  is the relative momentum and  $\sqrt{s}$  the center-of-momentum energy the two-particle system ( $s$  is the Mandelstam variable). The normalization of the standard two-particle states is given by

$$\langle \Omega', s'_1 \lambda'_1 s'_2 \lambda'_2 | \Omega, s_1 \lambda_1 s_2 \lambda_2 \rangle = \delta^{(2)}(\Omega' - \Omega) \delta_{s'_1 s_1} \delta_{\lambda'_1 \lambda_1} \delta_{s'_2 s_2} \delta_{\lambda'_2 \lambda_2} \quad (3.19)$$

This follows immediately from [Section 3.1](#). Next, to ensure that

$$\langle J' M' s'_1 \lambda'_1 s'_2 \lambda'_2 | JM s_1 \lambda_1 s_2 \lambda_2 \rangle = \delta_{J' J} \delta_{M' M} \delta_{s'_1 s_1} \delta_{\lambda'_1 \lambda_1} \delta_{s'_2 s_2} \delta_{\lambda'_2 \lambda_2} \quad (3.20)$$

we must have  $N_J = \sqrt{\frac{2J+1}{4\pi}}$ . Finally,

$$\langle \Omega, s'_1 \lambda'_1 s'_2 \lambda'_2 | J M s_1 \lambda_1 s_2 \lambda_2 \rangle = N_J D_{M\lambda}^{J*}(R_\Omega) \delta_{s'_1 s_1} \delta_{\lambda'_1 \lambda_1} \delta_{s'_2 s_2} \delta_{\lambda'_2 \lambda_2} \quad (3.21)$$

## Production Amplitudes

Given the two-particle helicity states, we can now construct production amplitudes which will model what we measure in the experiment.

We approach this with the  $S$ -matrix formalism. We assert that all of the dynamics of any reaction  $i \rightarrow f$  are elements of an invariant scattering matrix  $S$  written  $\langle f | S | i \rangle$ . We then define the matrix  $T$  such that  $S = 1 + 2iT$ , called the transition matrix<sup>1</sup>.

Let us examine the reaction  $a + b \rightarrow c + d$ . We can write the invariant  $S$ -matrix element as

$$\langle \vec{p}_c \lambda_c; \vec{p}_d \lambda_d | S | \vec{p}_a \lambda_a; \vec{p}_b \lambda_b \rangle = (4\pi)^2 \sqrt{\frac{s}{p_f p_i}} \langle \Omega \lambda_c \lambda_d | S(\sqrt{s}) | \varnothing \lambda_a \lambda_b \rangle \quad (3.22)$$

where we have used Equation (3.16) to write the states with an initial momentum  $(-)\vec{p}_i$  for particle  $(b)a$  pointing along the direction  $(\theta, \varphi) = (0, 0) \equiv \varnothing$  and a final momentum  $(-)\vec{p}_f$  for particle  $(d)c$  pointing in the direction  $\Omega$  with respect to  $\vec{p}_i$ . We can replace  $S$  with the definition of  $T$  to arrive at a similar formula for the invariant transition amplitude  $\mathcal{M}_{fi}$ ,

$$\mathcal{M}_{fi} = (4\pi)^2 \sqrt{\frac{s}{p_f p_i}} \langle \Omega \lambda_c \lambda_d | T(\sqrt{s}) | \varnothing \lambda_a \lambda_b \rangle \quad (3.23)$$

While we will not measure a cross-section exactly, we will roughly measure the number of events as a function of mass and helicity angles, which is proportional to the cross section. We refer to this as the “intensity” function (see Appendix B of [Chung Spin Formalisms](#)),

$$I(m, \Omega) \propto \frac{\partial^2 \sigma}{\partial m \partial \Omega} \equiv \frac{p_f}{p_i} \left| \frac{\mathcal{M}_{fi}}{8\pi \sqrt{s}} \right|^2 \quad (3.24)$$

We can also use this formalism to model two-body decays of the form  $c \rightarrow 1 + 2$ , where  $c$  has total angular momentum  $J$ . Starting in the rest frame of particle  $c$ , we say that particle (2)1 has momentum  $(-)\vec{p}$ , so the amplitude for a particular angular momentum  $M$  can be written as

---

<sup>1</sup>The factor of  $2i$  here is purely convention and makes some derivations more compact.

$$\langle \vec{p}\lambda_1; -\vec{p}\lambda_2 | \mathcal{M} | JM \rangle = \langle \vec{p}\lambda_1; -\vec{p}\lambda_2 | JM\lambda_1\lambda_2 \rangle \langle JM\lambda_1\lambda_2 | \mathcal{M} | JM \rangle \quad (3.25)$$

$$= 4\pi \sqrt{\frac{w}{p}} \underbrace{\langle \Omega\lambda_1; -\vec{p}\lambda_2 | JM\lambda_1\lambda_2 \rangle}_{N_J D_{M\lambda}^{J*}(\Omega)} \langle JM\lambda_1\lambda_2 | \mathcal{M} | JM \rangle \quad (3.26)$$

$$\equiv N_J D_{M\lambda}^{J*}(\Omega) F_{\lambda_1\lambda_2}^J \quad (3.27)$$

where  $w$  is the effective mass of the decaying particle,  $\lambda = \lambda_1 - \lambda_2$ , and we use the completeness relation  $\sum_{JM\lambda_1\lambda_2} |JM\lambda_1\lambda_2\rangle \langle JM\lambda_1\lambda_2| = 1$  along with Equation (3.21). We call  $F_{\lambda_1\lambda_2}^J$  the helicity decay amplitude.

If we wish to model  $X \rightarrow K_S^0 K_S^0$ , we first recognize that the kaon is a spin-0 particle, so the difference in helicity is  $\lambda = 0$ . Therefore,

$$I(m, \Omega) \propto |\mathcal{M}_{fi}|^2 \sim |N_J D_{M0}^{J*}(\Omega) F^J(m)|^2 = |Y_J^M(\Omega) F^J(m)|^2 \quad (3.28)$$

Since we cannot know the spin projection of a particle *a priori*, we will typically obtain it from fitting the intensity to a sum over these spherical harmonics, assigning an coefficient  $a_M^J$  to each and determining the spin from the best-fitting harmonic,

$$I(m, \Omega) \propto \left| \sum_{JM} a_M^J F^J(m) Y_J^M(\Omega) \right|^2 \quad (3.29)$$

It is important to remember here that  $\Omega$  has always been defined in terms of the helicity angles of the decay, i.e. the spherical angles with respect to the direction of particle  $X$ 's motion found after boosting to the helicity frame. This frame is defined as the rest-frame of  $X$  (found by boosting first from the lab frame to the center-of-momentum) with  $\hat{z}$  defined as the boost direction from the center-of-momentum frame,  $\hat{y}$  as normal to the production plane (the plane in which the beam and recoil proton move), and  $\hat{x} = \hat{y} \times \hat{z}$ .

### Including Linear Photon Polarization

As the GlueX beam has a known polarization, we can take advantage of this extra information to explore the parity exchanged in our reaction. Mathieu et al. [51] provide a derivation which begins with a slightly different representation of the scattering matrix, written in terms of spin-density matrix elements  $\rho_{\lambda\lambda'}^Y$  describing the coupling of a polarized photon to the helicity of the proton target (and that of the recoiling proton product):

$$I(m, \Omega) \propto \frac{p_f}{p_i} \left| \frac{\mathcal{M}_{fi}}{8\pi\sqrt{s}} \right|^2 = \kappa \sum_{\lambda\lambda'\lambda_p\lambda_{p'}} A_{\lambda;\lambda_p\lambda_{p'}}(m, \Omega) \rho_{\lambda\lambda'}^Y A_{\lambda';\lambda_1\lambda_2}^*(m, \Omega) \quad (3.30)$$

where

$$\kappa(m, s) = \frac{1}{(2\pi)^3} \frac{1}{4\pi} \frac{1}{2\pi} \frac{1}{2} \sqrt{\frac{\lambda(m^2, m_{K_S^0}^2, m_{K_S^0}^2)}{16m(s - m_p^2)^2}} \quad (3.31)$$

where  $\lambda(a, b, c) \equiv a^2 + b^2 + c^2 - 2(ab + bc + ca)^2$  and we define the reaction as  $\gamma p \rightarrow X p'$  with  $X \rightarrow K_S^0 K_S^0$ . Here, the indices  $\lambda$  and  $\lambda'$  couple the helicity of the incident photon to the amplitude  $A$ , while  $\lambda_p$  and  $\lambda_{p'}$  correspond to the helicity of the target and recoiling proton, respectively. Note that these nucleon helicities are not measured at GlueX, but we will keep them in our model for the sake of completeness. Additionally, since the Mandelstam variable  $s$  only shows up in this term, we will suppress its notation for now, but will bring it back at the end of the derivation.

The spin-density matrix for the photon,  $\rho_{\lambda\lambda'}^\gamma$ , can be written in terms of the polarization vector,

$$\rho_{\lambda\lambda'}^\gamma = \frac{1}{2} \left( I + \vec{P}_\gamma \cdot \vec{\sigma} \right) \quad (3.32)$$

where  $\vec{\sigma}$  are the Pauli matrices and

$$\vec{P}_\gamma = P_\gamma \begin{bmatrix} -\cos(2\Phi) \\ -\sin(2\Phi) \\ 0 \end{bmatrix} \quad (3.33)$$

for linearly polarized photons with polarization degree  $P_\gamma \in [0, 1]$  and polarization angle  $\Phi$  (measured with respect to the production plane). From here, we can expand the intensity into three terms,

$$I(m, \Omega, P_\gamma, \Phi) = I^0(m, \Omega) - P_\gamma I^1(m, \Omega) \cos(2\Phi) - P_\gamma(m, \Omega) \sin(2\Phi) \quad (3.34)$$

where

$$I^0(m, \Omega) = \frac{\kappa}{2} \sum_{\lambda\lambda_p\lambda_{p'}} A_{\lambda;\lambda_p\lambda_{p'}}(m, \Omega) A_{\lambda;\lambda_p\lambda_{p'}}^*(m, \Omega) \quad (3.35)$$

$$I^1(m, \Omega) = \frac{\kappa}{2} \sum_{-\lambda\lambda_p\lambda_{p'}} A_{\lambda;\lambda_p\lambda_{p'}}(m, \Omega) A_{\lambda;\lambda_p\lambda_{p'}}^*(m, \Omega) \quad (3.36)$$

$$I^2(m, \Omega) = i \frac{\kappa}{2} \sum_{\lambda\lambda_p\lambda_{p'}} \lambda A_{-\lambda;\lambda_p\lambda_{p'}}(m, \Omega) A_{\lambda;\lambda_p\lambda_{p'}}^*(m, \Omega) \quad (3.37)$$

Next, we can write

$$A_{\lambda;\lambda_p\lambda_{p'}} = a_{M;\lambda\lambda_p\lambda_{p'}}^J F_{\lambda\lambda_p\lambda_{p'}}^J(m) Y_J^M(\Omega) \quad (3.38)$$

---

<sup>2</sup>It is unfortunate that the notation for this function is typically written with a  $\lambda$ , and we will attempt to ensure the distinction from helicity is clear when we use it.

For clarity, we will absorb the coefficient  $a$  into the mass-dependent term  $F$  and define

$$T_{M;\lambda_p\lambda_{p'}}^J(m) \equiv a_{JM;\lambda_p\lambda_{p'}} F_{\lambda_p\lambda_{p'}}^J(m) \quad (3.39)$$

As mentioned, the polarization of the beam gives us access to information about the parity of the exchanged particle in the  $t$ -channel reaction. For this, we work in the “reflectivity” basis,

$$T_{M;\lambda_p\lambda_{p'}}^{J(\epsilon)}(m) \equiv \frac{1}{2} \left[ T_{M;+,\lambda_p\lambda_{p'}}^J(m) - \epsilon(-1)^M T_{M;-,\lambda_p\lambda_{p'}}^J(m) \right] \quad (3.40)$$

This basis is useful, as it can be shown that in the high-energy limit, the reflectivity  $\epsilon = \pm 1$  corresponds to the exchanged naturality in  $t$ -channel reactions<sup>3</sup>. Furthermore, parity invariance leads to the relation

$$T_{M;-\lambda_p-\lambda_{p'}}^{J(\epsilon)}(m) = \epsilon(-1)^{\lambda_p-\lambda_{p'}} T_{M;\lambda_p\lambda_{p'}}^{J(\epsilon)}(m) \quad (3.41)$$

so there are really only two unique partial waves, those where the proton helicity flips ( $\eta = -1$ ) and those where it does not ( $\eta = +1$ ), which we will write as  $T_{M;\eta}^{J(\epsilon)}$ :

$$T_{M;+}^{J(\epsilon)}(m) \equiv T_{M;+,+}^{J(\epsilon)}(m) \quad T_{M;-}^{J(\epsilon)}(m) \equiv T_{M;+,-}^{J(\epsilon)}(m) \quad (3.42)$$

### 3.2 The $Z_\ell^m$ Amplitude

The next part of the derivation pertains to both how we formulate this amplitude in practice and how we define sets of waves with which to fit our data, and it closely follows the work of [Shepherd GlueXdoc4094](#).

We can rewrite the intensity function in [Equation \(3.34\)](#) in terms of exponentials. We will also expand out the sums over  $\lambda = \pm$ , the photon helicity, and temporarily suppress the indices of nucleon helicity for clarity (although I will keep the sum to remind us that these indices exist on each  $A$ ).

$$I(m, \Omega, P_Y, \Phi) = \frac{\kappa}{2} \sum_{\lambda_p\lambda_{p'}} \left[ A_-(m, \Omega) A_-^*(m, \Omega) + A_+(m, \Omega) A_+^*(m, \Omega) - P_Y e^{i2\Phi} A_-(m, \Omega) A_+^*(m, \Omega) - P_Y e^{-i2\Phi} A_+(m, \Omega) A_-^*(m, \Omega) \right] \quad (3.43)$$

Next, we define polarized amplitudes,

$$\tilde{A}_\pm(m, \Omega, \Phi) \equiv e^{\mp i\Phi} A_\pm(m, \Omega), \quad (3.44)$$

---

<sup>3</sup>i.e. Positive reflectivity implies natural parity exchange and negative reflectivity implies unnatural parity exchange

so that the intensity can be written as

$$\frac{\kappa}{4} \sum_{\lambda_p \lambda_{p'}} \left[ (1 - P_\gamma) \left| \tilde{A}_+(m, \Omega, \Phi) + \tilde{A}_-(m, \Omega, \Phi) \right|^2 + (1 + P_\gamma) \left| \tilde{A}_+(m, \Omega, \Phi) - \tilde{A}_-(m, \Omega, \Phi) \right|^2 \right] \quad (3.45)$$

Rewriting these polarized amplitudes in terms of those of Equation (3.40), we find

$$\tilde{A}_+(m, \Omega, \Phi) = \sum_{\lambda_p \lambda_{p'}} \sum_{J, M} [T_M^{J(-)}(m) + T_M^{J(+)}(m)] e^{-i\Phi} Y_J^M(\Omega) \quad (3.46)$$

$$\tilde{A}_-(m, \Omega, \Phi) = \sum_{\lambda_p \lambda_{p'}} \sum_{J, M} [T_M^{J(-)}(m) - T_M^{J(+)}(m)] e^{-i\Phi} Y_J^{M*}(\Omega) \quad (3.47)$$

$$(3.48)$$

We now define the function,

$$\hat{Z}_J^M(\Omega, \Phi) \equiv e^{-i\Phi} Y_J^M(\Omega) \quad (3.49)$$

This allows us to rewrite Equation (3.45) as

$$I(m, \Omega, P_\gamma, \Phi) = \sum_{\lambda_p \lambda_{p'}} \kappa \left\{ (1 - P_\gamma) \left| T_M^{J(-)}(m) \text{Re}[\hat{Z}_J^M(\Omega, \Phi)] + i T_M^{J(+)}(m) \text{Im}[\hat{Z}_J^M(\Omega, \Phi)] \right|^2 \right. \quad (3.50)$$

$$\left. + (1 + P_\gamma) \left| T_M^{J(+)}(m) \text{Re}[\hat{Z}_J^M(\Omega, \Phi)] + i T_M^{J(-)}(m) \text{Im}[\hat{Z}_J^M(\Omega, \Phi)] \right|^2 \right\} \quad (3.51)$$

$$(3.52)$$

Next, we recognize the parity invariance mentioned in Equation (3.41) to transform the intensity into four coherent sums. To demonstrate this, we will show the expansion of the first coherent sum given in Equation (3.52), suppressing  $m, \Omega$  and  $\Phi$  for simplicity:

$$\begin{aligned} & \sum_{\lambda_p \lambda_{p'}} \left| \sum_{JM} \left( T_{M; \lambda_p \lambda_{p'}}^{J(-)} \text{Re}[\hat{Z}_J^M] + i T_{M; \lambda_p \lambda_{p'}}^{J(+)} \text{Im}[\hat{Z}_J^M] \right) \right|^2 \\ &= \sum_{\lambda_p \lambda_{p'}} \sum_{JM} \sum_{J'M'} \left( T_{M; \lambda_p \lambda_{p'}}^{J(-)} \text{Re}[\hat{Z}_J^M] + i T_{M; \lambda_p \lambda_{p'}}^{J(+)} \text{Im}[\hat{Z}_J^M] \right) \left( T_{M'; \lambda_p \lambda_{p'}}^{J'(-)*} \text{Re}[\hat{Z}_{J'}^{M'}] + i T_{M'; \lambda_p \lambda_{p'}}^{J'(+)*} \text{Im}[\hat{Z}_{J'}^{M'}] \right) \\ &= \sum_{\lambda_p \lambda_{p'}} \sum_{JM} \sum_{J'M'} \left\{ \left( T_{M; \lambda_p \lambda_{p'}}^{J(-)} T_{M'; \lambda_p \lambda_{p'}}^{J'(-)*} \text{Re}[\hat{Z}_J^M] \text{Re}[\hat{Z}_{J'}^{M'}] \right) - \left( T_{M; \lambda_p \lambda_{p'}}^{J(+)} T_{M'; \lambda_p \lambda_{p'}}^{J'(+)*} \text{Im}[\hat{Z}_J^M] \text{Im}[\hat{Z}_{J'}^{M'}] \right) \right. \\ & \quad \left. + i \left( T_{M; \lambda_p \lambda_{p'}}^{J(-)} T_{M'; \lambda_p \lambda_{p'}}^{J'(+)*} \text{Re}[\hat{Z}_J^M] \text{Im}[\hat{Z}_{J'}^{M'}] \right) + i \left( T_{M; \lambda_p \lambda_{p'}}^{J(+)} T_{M'; \lambda_p \lambda_{p'}}^{J'(-)*} \text{Im}[\hat{Z}_J^M] \text{Re}[\hat{Z}_{J'}^{M'}] \right) \right\} \end{aligned} \quad (3.53)$$

Next, we use the relation

$$\sum_{\lambda_p \lambda_{p'}} T_{M; \lambda_p \lambda_{p'}}^{J(\epsilon)} T_{M'; \lambda_p \lambda_{p'}}^{J'(\epsilon')*} = (1 + \epsilon \epsilon') \sum_{\eta} T_{M; \eta}^{J(\epsilon)} T_{M'; \eta}^{J'(\epsilon')*} \quad (3.54)$$

from parity conservation, which causes the last two terms in Equation (3.53) to vanish. The remaining terms can be rewritten as coherent sums, yielding the following expression for the intensity:

$$I(m, \Omega, P_\gamma, \Phi) = 2\kappa \sum_{\eta} \left\{ (1 - P_\gamma) \left| \sum_{JM} T_{M;\eta}^{J(-)}(m) \text{Re}[\hat{Z}_J^M(\Omega, \Phi)] \right|^2 + (1 - P_\gamma) \left| \sum_{JM} T_{M;\eta}^{J(+)}(m) \text{Im}[\hat{Z}_J^M(\Omega, \Phi)] \right|^2 \right. \\ \left. + (1 + P_\gamma) \left| \sum_{JM} T_{M;\eta}^{J(+)}(m) \text{Re}[\hat{Z}_J^M(\Omega, \Phi)] \right|^2 + (1 + P_\gamma) \left| \sum_{JM} T_{M;\eta}^{J(-)}(m) \text{Im}[\hat{Z}_J^M(\Omega, \Phi)] \right|^2 \right\} \quad (3.55)$$

We can absorb the factors of  $(1 \pm P_\gamma)$  by defining the function

$$Z_J^{M(\pm)}(\Omega, P_\gamma, \Phi) = (\sqrt{1 \pm P_\gamma} + i\sqrt{1 \mp P_\gamma}) \hat{Z}_J^M(\Omega, \Phi) \quad (3.56)$$

We finally note that in the energy range of this reaction, we do not expect to make states with additional angular momentum  $L$ , so for our interests,  $J$  corresponds to spin. However, to be consistent with common nomenclature on this topic, we will use the notation  $(\ell, m)$  in lieu of  $(J, M)$  and consider  $\ell$  to correspond to spin. Previously, it was mentioned that we have no way to measure the helicity of the proton before or after this reaction, so in practice we ignore the summation over  $\eta$ . However, we should be cautious of the phase-space factor  $\kappa$ , as it depends on both  $m$  and  $s$ . This is not an issue in (mass) binned fits, which we will see later, as we average over  $m$  anyway and assume the bins are small enough that  $s$  does not vary much in each bin, but this term is non-negligible in mass-dependent formulations.

$$I(m, s, \Omega, P_\gamma, \Phi) = 2 \sum_{\eta} \left\{ \left| \sum_{JM} \hat{T}_{M;\eta}^{J(-)}(m, s) \text{Re}[Z_J^M(\Omega, P_\gamma, \Phi)] \right|^2 + \left| \sum_{JM} \hat{T}_{M;\eta}^{J(+)}(m, s) \text{Im}[Z_J^M(\Omega, P_\gamma, \Phi)] \right|^2 \right. \\ \left. + \left| \sum_{JM} \hat{T}_{M;\eta}^{J(+)}(m, s) \text{Re}[Z_J^M(\Omega, P_\gamma, \Phi)] \right|^2 + \left| \sum_{JM} \hat{T}_{M;\eta}^{J(-)}(m, s) \text{Im}[Z_J^M(\Omega, P_\gamma, \Phi)] \right|^2 \right\} \quad (3.57)$$

where  $\hat{T}_{M;\eta}^{J(\epsilon)}(m, s) \equiv \kappa^2(m, s) T_{M;\eta}^{J(\epsilon)}(m)$

Finally, we can choose a parameterization for  $\hat{T}_{M;\eta}^{J(\epsilon)}(m, s) \rightarrow \hat{T}_{M;\eta}^{J(\epsilon)}(\vec{\beta}; m, s)$ . These  $\vec{\beta} \in \mathbb{C}^d$  are free parameters in our models.

This gives us a generalized intensity function for linearly polarized photoproduction,

$$\mathcal{I}(\vec{\beta}; m, s, \Omega, P_\gamma, \Phi) = 2 \sum_{\eta} \left\{ \left| \sum_{JM} \hat{T}_{M;\eta}^{J(-)}(\vec{\beta}; m, s) \text{Re}[Z_J^M(\Omega, P_\gamma, \Phi)] \right|^2 + \left| \sum_{JM} \hat{T}_{M;\eta}^{J(+)}(\vec{\beta}; m, s) \text{Im}[Z_J^M(\Omega, P_\gamma, \Phi)] \right|^2 \right. \\ \left. + \left| \sum_{JM} \hat{T}_{M;\eta}^{J(+)}(\vec{\beta}; m, s) \text{Re}[Z_J^M(\Omega, P_\gamma, \Phi)] \right|^2 + \left| \sum_{JM} \hat{T}_{M;\eta}^{J(-)}(\vec{\beta}; m, s) \text{Im}[Z_J^M(\Omega, P_\gamma, \Phi)] \right|^2 \right\} \quad (3.58)$$

The simplest model we can parameterize is one in which we bin the data in mass  $m$  and let  $T_{M;\eta}^{J(\epsilon)}(\vec{\beta}; m) = \beta_i$  for the  $i$ th mass bin. This is equivalent to modeling the mass dependence as a piecewise function where each segment is



constant. We will discuss such parameterizations in [Section 4.2](#). In the next section, we will discuss a more complex mass-dependent parameterization.

### 3.3 The $K$ -Matrix Parameterization

If we wish to parameterize the amplitude  $T(m)$  as a function of mass, there are several options. Perhaps the most ubiquitous is the resonant lineshape devised by Breit and Wigner in 1936 [52] whose amplitude can be written as a function of the invariant mass  $m$ ,

$$T(m; M, \Gamma) = \frac{M\Gamma / \sqrt{\pi}}{(M^2 - m^2) - iM\Gamma} \quad (3.59)$$

where  $M$  and  $\Gamma$  describe the centroid and width of the peak respectively. We typically relate the centroid to the mass of the resonance and the width to the inverse of the lifetime. This is the non-relativistic form, and we can see that

$$|T(m; M, \Gamma)|^2 = \frac{(M\Gamma)^2 / \pi}{(m^2 - M^2)^2 + (M\Gamma)^2} \quad (3.60)$$

which can be seen to be a Cauchy distribution.

We could continue in this way and define the mass-dependent dynamics of our system as a sum of Breit-Wigner distributions. However, this is not the correct approach, as we will show that this does not preserve the unitarity of the  $S$ -matrix. Let us examine an alternate formulation, which we will call the  $K$ -matrix method. We will see that this  $K$ -matrix yields a Breit-Wigner for a single resonance in a single decay channel, but it can be extended to multiple resonances in multiple channels while preserving unitarity.

Following the derivation by Chung et al. [53], we begin with our definition of the transition operator from [Section 3.1](#),

$$S = I + 2iT \quad (3.61)$$

To conserve probability, we require the  $S$  matrix to be unitary, i.e.  $SS^\dagger = S^\dagger S = I$ . Plugging in the definition of  $T$ , we see that

$$\begin{aligned} I &= (I + 2iT)(I - 2iT^\dagger) \\ I &= I + 2TT^\dagger + 2iT - 2iT^\dagger \\ T - T^\dagger &= 2iTT^\dagger \end{aligned} \quad (3.62)$$

We then by the inverse of each matrix,

$$\begin{aligned}
T(T^\dagger)^{-1} - I &= 2iI \\
(T^\dagger)^{-1} - T^{-1} &= 2iI \\
(T^{-1} + iI)^\dagger &= T^{-1} + iI
\end{aligned} \tag{3.63}$$

Next, we introduce the  $K$ -matrix, defined as

$$K^{-1} = T^{-1} + iI \tag{3.64}$$

$K$  is Hermitian by Equation (3.63), and by time reversal invariance of  $T$ ,  $K$  must be symmetric. For simplicity, we can also choose  $K \in \mathbb{R}^n$ . Continuing from the previous equation,

$$\begin{aligned}
I &= T^{-1}K + iK \\
T &= K + iTK
\end{aligned} \tag{3.65}$$

However, we could also reverse the order of multiplication here,

$$\begin{aligned}
K^{-1}T &= I + iT \\
T &= K + iKT
\end{aligned} \tag{3.66}$$

Therefore,  $K$  and  $T$  commute. Furthermore, we can solve for  $T$  to find

$$\begin{aligned}
T - iTK &= K \\
T(I - iK) &= K \\
T &= K(I - iK)^{-1}
\end{aligned} \tag{3.67}$$

For a single channel, the  $S$ -matrix is scalar and can be written in the form  $S = e^{2i\delta}$ .

An Argand diagram plots the real and imaginary parts of  $T$  in the complex plane. By the definition of  $T$  along with this definition of  $S$ , unitarity-preserving trajectories for  $T$  must lie within a circle of radius  $1/2$  centered at  $0 + \frac{1}{2}i$ , which we refer to as the unitary circle. Since  $K$  is defined from a unitary  $T$ - and  $S$ -matrix, it will always preserve unitarity as long as its properties of Hermiticity and symmetry are met. Therefore, any real symmetric  $K$ -matrix will yield a unitary  $S$ -matrix.

Next, we must choose how to parameterize this  $K$ -matrix and write it in a Lorentz-invariant form.

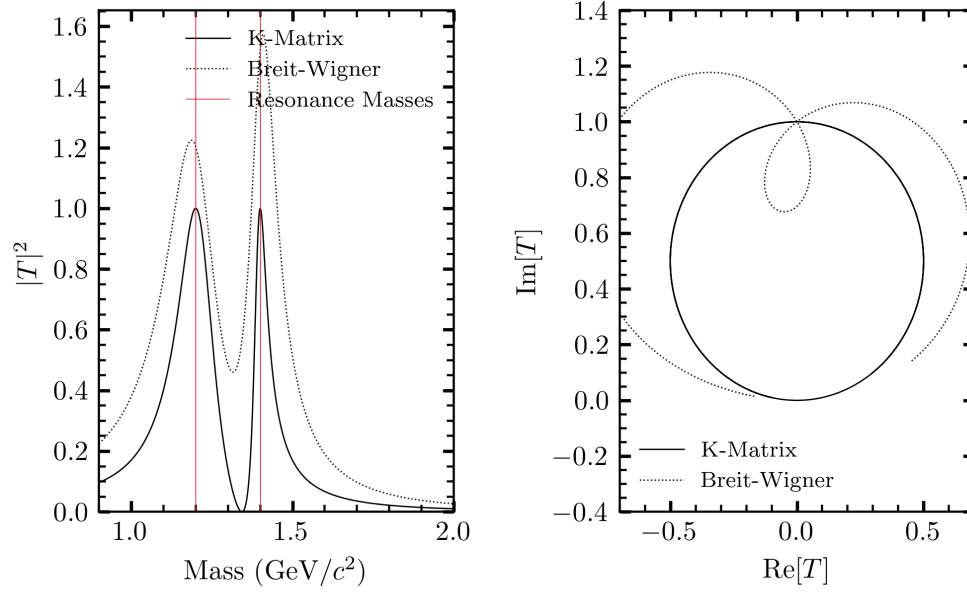


**Figure 3.1:** An Argand diagram depicting two fictitious resonances with masses of  $1.2 \text{ GeV}/c^2$  and  $1.4 \text{ GeV}/c^2$  and widths of  $200 \text{ MeV}/c^2$  and  $100 \text{ MeV}/c^2$  respectively using both the  $K$ -matrix formalism and interfering Breit-Wigners. The  $T$ -matrix formed from Breit-Wigners exceeds the unitary circle, implying that this construction breaks unitarity, while the  $K$ -matrix does not.

### Resonances as Poles of the $K$ -matrix

Resonances can be parametrized either as constant elements in the  $K$ -matrix, which are usually interpreted as “molecular” resonances resulting from the exchange of force-carrying bosons, or from poles, which are thought of as the resonances describing decaying hadrons [54]. While we are more interested in the second case, we will include a linear combination of poles and constant terms in the parameterization, as follows:

$$K_{ij}(m) = \sum_{\alpha} \frac{g_{\alpha i}(m)g_{\alpha j}(m)}{m_{\alpha}^2 - m^2} + c_{ij} \quad (3.68)$$

Here,  $\alpha$  indexes the resonances, with  $m_{\alpha}$  corresponding to the pole mass<sup>4</sup> of the  $\alpha$ th resonance and  $g_{\alpha i}$  corresponding to a term coupling the  $\alpha$ th resonance to the  $i$ th decay channel.  $c_{ij}$  denotes any constant terms mentioned in the previously.

For a single resonance in a single channel, we can write the  $T$ -matrix as

$$T = K(I - iK)^{-1} \quad (3.69)$$

$$= \frac{\frac{g^2(m)}{m_{\alpha}^2 - m^2}}{1 - i \left( \frac{g^2(m)}{m_{\alpha}^2 - m^2} \right)} \quad (3.70)$$

<sup>4</sup>This is not necessarily the same value as the centroid of a Breit-Wigner fit to the same data.

$$= \frac{g^2(m)}{m_\alpha^2 - m^2 - ig^2(m)} \quad (3.71)$$

which we see is identical to the Breit-Wigner form given in Equation (3.59) with  $g^2(m) = m_\alpha \Gamma_\alpha(m)$ <sup>5</sup>.

Furthermore, we can now demonstrate the fundamental reason why we need to use the  $K$ -matrix in lieu of Breit-Wigners when describing multiple overlapping resonances. Figure 3.1 shows that, even in a single channel, two interfering Breit-Wigners do not preserve unitarity, while the corresponding  $K$ -matrix does.

In the case where a resonance can decay into multiple channels, we say that  $\Gamma_\alpha(m) = \sum_i \Gamma_{\alpha i}(m)$  is the total width and  $\Gamma_{\alpha i}(m)$  are called the partial widths. In the relativistic form of the Breit-Wigner (and the Lorentz-invariant form of the resulting  $S$ -matrix), widths (and therefore partial widths) are given by

$$\Gamma_{\alpha i} = \gamma_{\alpha i}^2 \Gamma_\alpha B_{\alpha i}^\ell(m) \sqrt{\rho_i(m)} \quad (3.72)$$

where  $\gamma_{\alpha i}^2$  is the fraction of the total width<sup>6</sup>,  $\Gamma_\alpha$ , which is coupled to the channel  $i$ , and  $\rho_i(m)$  is the phase space factor

$$\rho_i(m) = \sqrt{\chi_i^+(m) \chi_i^-(m)} \quad \text{where} \quad \chi_i^\pm = 1 - \left( \frac{m_1 \pm m_2}{m} \right)^2 \quad (3.73)$$

when the  $i$ th channel describes the decay  $\alpha \rightarrow 1 + 2$  and  $B_{\alpha i}^\ell(m)$  is the centrifugal barrier factor describing the suppression to the partial width when a resonance has angular momentum  $\ell$ . We typically parameterize this via form factors derived by Blatt and Weisskopf [55],

$$B_{\alpha i}^\ell(m) = \frac{F_\ell(z_i(m))}{F_\ell(z_i(m_\alpha))} \quad (3.74)$$

$$z_i(m) \equiv \left( \frac{q_i(m)}{q_R} \right)^2 \quad (3.75)$$

$$F_0(z) = 1 \quad (3.76)$$

$$F_1(z) = \sqrt{\frac{2z}{z+1}} \quad (3.77)$$

$$F_2(z) = \sqrt{\frac{13z^2}{(z-3)^2 + 9z}} \quad (3.78)$$

$$F_\ell(z) = \sqrt{\frac{|h_\ell^{(1)}(1)|^2}{z |h_\ell^{(1)}(\sqrt{z})|^2}} \quad (3.79)$$

<sup>5</sup>Here,  $\Gamma$  depends on  $m$ , which is true for a relativistic form of the Breit-Wigner amplitude.

<sup>6</sup>However,  $\gamma_{\alpha i}$  may itself be negative so long as it is purely real.

where  $q_i(m) = m\rho_i(m)/2$  is the breakup momentum for the  $i$ th channel<sup>7</sup>,  $q_R$  is the impact parameter/interaction radius (we use 0.1973 GeV in our calculations), and  $h_\ell^{(1)}$  is a spherical Hankel function of the first kind (see Equation 2.4 of [56])

For clarity, we typically reparameterize these partial widths such that

$$g_{ai}(m) = g_{ai}B_{ai}^\ell(m)\sqrt{\rho_i(m)} \quad (3.80)$$

so we can define the Lorentz-invariant  $K$ -matrix,  $\hat{K}$ , as

$$K_{ij}(m) = \sqrt{\rho_i(m)} \left( \sum_\alpha B_{ai}^\ell(m) \left[ \frac{g_{ai}g_{aj}}{m_\alpha^2 - m^2} + \sum_n \bar{c}_{nij}m^{2n} \right] B_{aj}^\ell(m) \right) \sqrt{\rho_j(m)} \quad (3.81)$$

$$K_{ij}(m) = \sqrt{\rho_i(m)} \hat{K}_{ij}(m) \sqrt{\rho_j(m)} \quad (3.82)$$

where we have absorbed some multiplicative factors into  $c_{ij}$  to form the series expansion over powers of  $m^2$  (since  $\rho(m)$  and  $B_{ai}^\ell(m)$  only contain even powers of  $m$ ) with coefficients  $\bar{c}_{ij}$ . Here,  $\bar{K}$  replaces  $K$  in Equation (3.67) as an intermediate step to defining a Lorentz-invariant formulation.

According to Chung<sup>8</sup>, the Lorentz-invariant form of the  $T$ -matrix,  $\hat{T}$  can be written as

$$T = \sqrt{\rho} \hat{T} \sqrt{\rho} \quad (3.83)$$

where we define the notation

$$\rho_{ij}(m) \equiv \rho_i(m)\delta_{ij} \quad (3.84)$$

$$\sqrt{\rho_{ij}(m)} \equiv \sqrt{\rho_i(m)}\delta_{ij} \quad (3.85)$$

In terms of Equations (3.64), (3.67) and (3.82), we can write

$$\hat{K}^{-1} = \hat{T}^{-1} + \imath\rho \quad (3.86)$$

Following the previous derivation with these invariant forms, we find that

$$\hat{T} = (I - \imath\hat{K}\rho)^{-1}\hat{K} \quad (3.87)$$

<sup>7</sup>i.e. the magnitude of the momentum either decay product will have in the rest frame of the decay

<sup>8</sup>cite: S. U. Chung, Spin Formalisms, CERN Yellow Report, CERN (1971) 71-78

### Production Amplitudes from a $K$ -Matrix

The  $T$ -matrix given in Equation (3.87) describes  $s$ -channel resonances (as in  $a + b \rightarrow X \rightarrow c + d$ ). We can transform this into a production amplitude following Aitchison [57]:

$$\hat{F} = (I - i\hat{K}\rho)^{-1}\hat{P} \quad (3.88)$$

where

$$\hat{P}_i(\vec{\beta}; m) = \sum_{\alpha} \left( \frac{\beta_{\alpha} g_{\alpha i}}{m_{\alpha}^2 - m^2} + \sum_n c_{ni} m^{2n} \right) B_{\alpha i}^{\ell}(m) \quad (3.89)$$

Here,  $\beta_{\alpha}$  describes the complex coupling from the initial state to the resonance  $\alpha$ . This can be thought of like a coupling coefficient in front of a single Breit-Wigner. The polynomial of coefficients are included for completeness, as any constant terms in  $P$  preserve unitarity in the same way as constant terms in  $K$ , and the division of the factor of  $\rho_i(m) \sim \rho_i(m^2)$  from Equation (3.80) and  $B_{\alpha i}^{\ell}(m) \sim B_{\alpha i}^{\ell}(m^2)$  creates the given form.

### The Chew-Mandelstam Matrix

For reasons which will become clear, we will define the diagonal matrix  $C$ , called the Chew-Mandelstam matrix, with the property

$$\text{Im}[C(m)] = -\rho(m) \quad \text{or} \quad C(m) = A(m) - i\rho(m) \quad (3.90)$$

for some real function  $A(m)$ . It can be shown that we can replace  $-i\rho$  in Equation (3.87) with such a matrix  $C$  and still retain a valid  $K$ -matrix representation [58],

$$\hat{T} = (I + \hat{K}C)^{-1}\hat{K} \quad (3.91)$$

and

$$\hat{F} = (I + \hat{K}C)^{-1}\hat{P} \quad (3.92)$$

The exact form of  $A(m)$  is arbitrary, but we will be using

$$C_{ii}(m) = C((m_1 + m_2)^2) + \frac{\rho_i(m)}{\pi} \ln \left[ \frac{\chi_i^+(m) + \rho_i(m)}{\chi_i^+(m) - \rho_i(m)} \right] - \frac{\chi_i^+(m)}{\pi} \frac{m_2 - m_1}{m_1 + m_2} \ln \frac{m_2}{m_1} \quad (3.93)$$

where  $m_1$  and  $m_2$  are the masses of the final state of the  $i$ th decay channel, and we can choose  $C((m_1 + m_2)^2) = 0$  for normalization. See [59], [60], [61], and [62] for derivations and additional details of this expression. The motivation for this choice is that it is better behaved below threshold than  $\rho(m)$ , as can be seen in Figure 3.2.

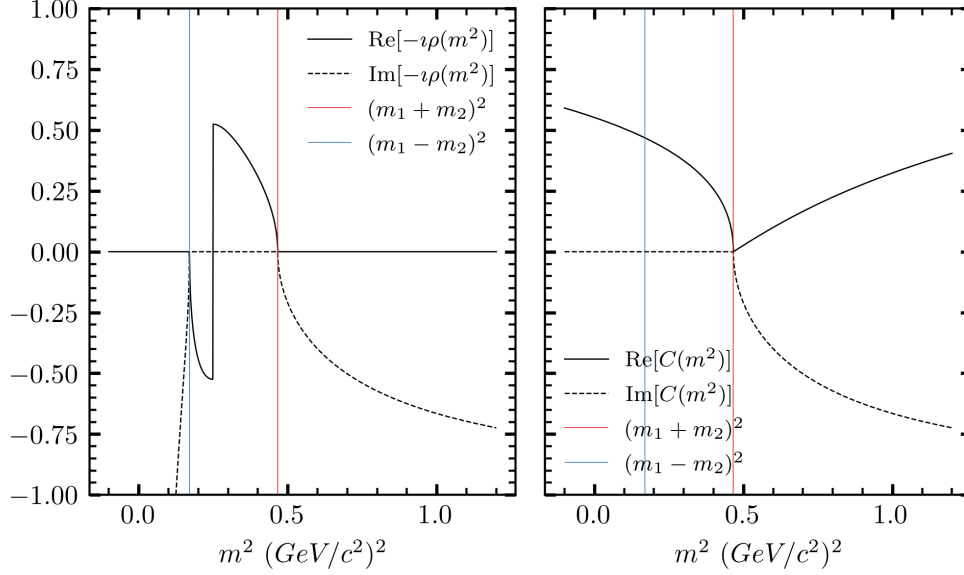


**Figure 3.2:** A comparison of the normal phase-space function,  $\rho(m)$  (left) and the Chew-Mandelstam matrix,  $C(m)$  (right) on the  $\pi^0\eta$  channel. Both functions have the same imaginary part above the threshold  $m = m_1 + m_2$ , but phase-space function has discontinuities and singularities below the threshold.

The impetus of this complication is that this particular formulation of the Chew-Mandelstam matrix is used in [63] and [64]. We do not have enough data to constrain the pole positions of every resonance in this channel (as we only have access to one of several channels used in those papers), so we will use the  $K$ -matrix coefficients ( $g_{i\alpha}$  and  $m_\alpha$ ) from their coupled-channel analysis of data from the Crystal Barrel and COMPASS experiments as fixed values in our analysis, fitting only the couplings ( $\vec{\beta}$ ) to photoproduction. Additionally, using the results from these papers requires a Adler zero term in front of the  $K$ -matrix for the  $f_0$  mesons of the form  $\frac{(s-s_0)}{s_{\text{norm}}}$ , where they use  $s_0 = m_{\pi_0}^2/2$  and  $s_{\text{norm}} = 1$ .

We can then combine Equation (3.92) with Equation (3.58), choosing  $T_{M;\eta}^{J(\epsilon)}(\vec{\beta}; m) = \hat{F}(\vec{\beta}; m)$ , to form a mass-dependent model of polarized photoproduction for the  $K_S^0 K_S^0$  channel which will be further discussed in Section 4.3.

### 3.4 Waveset Selection





## Chapter 4

# Results and Systematic Studies

### 4.1 Fitting Methods

To fit the aforementioned models to the data, we employ an algorithm which maximizes the likelihood function,

$$\mathcal{L}(\vec{\beta}) = e^{-\mathcal{N}} \frac{\mathcal{N}^N}{N!} \prod_{i=1}^N \mathcal{P}_i(\vec{\beta}) \quad (4.1)$$

where  $N$  is the number of events in the data,  $\mathcal{N}$  is the number of events predicted by the model, and  $\mathcal{P}_i(\vec{\beta})$  is the normalized probability distribution function evaluated on the  $i$ th event at position  $\vec{\beta}$  in parameter space. The term in front of the product is a Poisson distribution which describes the “extended” maximum likelihood method. We relate these probability distributions to our modeled intensity function in [Equation \(3.58\)](#) via the normalization,

$$\mathcal{I}(\vec{\beta}; m_i, s_i, \Omega_i, P_{Y,i}, \Phi_i) \equiv \mathcal{I}_i(\vec{\beta}) = \mathcal{N} \mathcal{P}_i(\vec{\beta}) \quad (4.2)$$

h

By absorbing the factor of  $\mathcal{N}^N$  into the product, we find

$$\mathcal{L}(\vec{\beta}) = \frac{e^{-\mathcal{N}}}{N!} \prod_{i=1}^N \mathcal{I}_i(\vec{\beta}) \quad (4.3)$$

We want to maximize this function, but the product makes this computationally difficult and unstable, since it can grow very large (if  $\mathcal{I} > 1$ ) or very small (if  $\mathcal{I} < 1$ ) to a point where its value exceeds floating-point precision. The standard solution is to instead minimize the negative logarithm of the likelihood instead,

$$-2 \ln \mathcal{L}(\vec{\beta}) = -2 \left( \sum_{i=1}^N \left[ \ln \mathcal{I}_i(\vec{\beta}) \right] - \mathcal{N} - \ln N! \right) \quad (4.4)$$

where the factor of two scales the log-likelihood to correspond to a  $\chi^2$  distribution as  $N \rightarrow \infty$  by Wilks’ theorem, allowing us to obtain an accurate covariance matrix from the fit for uncertainty estimation.

In an ideal world, we could stop here, ignoring the last two terms as they are constant in  $\beta$  and therefore do not contribute to the gradient of the negative log-likelihood. However, we must also consider the efficiency of the detector itself, which we will define as  $\eta(m_i, s_i, \Omega_i, P_{\gamma,i}, \Phi_i) \equiv \eta_i$ . In principle, we do not know the analytical form of this function, but we will later see that we can approximate it using Monte Carlo simulated data.

With this efficiency function in mind, we find that  $\mathcal{N}$ , the normalization factor which describes the number of events predicted by the model, becomes

$$\mathcal{N} = \int d\vec{x} \mathcal{I}(\vec{\beta}; \vec{x}) \eta(\vec{x}) \quad (4.5)$$

where  $\vec{x} = (m, s, \Omega, P_\gamma, \Phi)$ . This means we can write the normalized probability distribution functions as

$$\mathcal{P}_i(\vec{\beta}) = \frac{1}{\mathcal{N}} \mathcal{I}_i(\vec{\beta}) \eta_i \quad (4.6)$$

This changes the negative log-likelihood to

$$-2 \ln \mathcal{L}(\vec{\beta}) = -2 \left( \sum_{i=1}^N [\ln \mathcal{I}_i(\vec{\beta})] - \int d\vec{x} \mathcal{I}(\vec{\beta}; \vec{x}) \eta(\vec{x}) - \ln N! + \sum_{i=1}^N [\ln \eta_i] \right) \quad (4.7)$$

$$= -2 \left( \sum_{i=1}^N [\ln \mathcal{I}_i(\vec{\beta})] - \int d\vec{x} \mathcal{I}(\vec{\beta}; \vec{x}) \eta(\vec{x}) \right) + C \quad (4.8)$$

Next, we need a way of dealing with the integral term, particularly with the  $\eta(\vec{x})$  function for which we do not have access to the analytical form. To approximate this integral, we use both the fundamental theorem of calculus and the mean value theorem for derivatives, which together relate the integral of a function to its average value on the domain of integration,

$$\int_{\mathcal{D}} f(\vec{x}) d\vec{x} = \mathcal{A} \langle f(\vec{x}) \rangle \quad (4.9)$$

where  $\mathcal{A}$  is the area of the integration domain  $\mathcal{D}$  and  $\langle f(\vec{x}) \rangle$  denotes the average value of  $f(\vec{x})$  on that domain. If we generate phase-space Monte Carlo for the  $K_S^0 K_S^0$  channel, we can model  $\eta(\vec{x})$  as an indicator function corresponding to whether or not an event is detected by a simulation of the detector, passes through the reconstruction process described in [Section 2.1](#), and passes through our finer data selection from [Section 2.2](#). We can then write the average as a sum over the “accepted” Monte Carlo events,

$$\int d\vec{x} \mathcal{I}(\vec{\beta}; \vec{x}) \eta(\vec{x}) = \frac{1}{\mathcal{A} N_g} \sum_{j=1}^{N_a} [\mathcal{I}_j(\vec{\beta})] \quad (4.10)$$

where  $\mathcal{I}_j(\vec{\beta})$  is evaluated on the  $j$ th accepted Monte Carlo event<sup>1</sup>, and  $N_a$  and  $N_g$  are the number of accepted and generated events, respectively. We still need to deal with the factor of  $A$ . We could absorb this into our intensity function by scaling the intensity by  $A^{N_a}$ , which would eliminate it from this term. In the data term, we would then have

$$\sum_{i=1}^N \left[ A^{N_a} \mathcal{I}_i(\vec{\beta}) \right] = \sum_{i=1}^N \left[ \mathcal{I}_i(\vec{\beta}) \right] + N N_a \ln A \quad (4.11)$$

where the new additive term is constant in  $\vec{\beta}$  and can again be ignored in the minimization. At this stage, we need to minimize

$$-2 \ln \mathcal{L}(\vec{\beta}) = -2 \left( \sum_{i=1}^N \left[ \ln \mathcal{I}_i(\vec{\beta}) \right] - \frac{1}{N_g} \sum_{i=j}^{N_a} \left[ \mathcal{I}_j(\vec{\beta}) \right] \right) \quad (4.12)$$

We can incorporate event weights (from accidental subtraction or sPlot, for example) into these sums as

$$-2 \ln \mathcal{L}(\vec{\beta}) = -2 \left( \sum_{i=1}^N \left[ w_i \ln \mathcal{I}_i(\vec{\beta}) \right] - \frac{1}{N_g} \sum_{i=j}^{N_a} \left[ w_j \mathcal{I}_j(\vec{\beta}) \right] \right) \quad (4.13)$$

An additional scaling of the intensity with  $\mathcal{I}(\vec{\beta}) \rightarrow \varepsilon^{-N_a} \mathcal{I}(\vec{\beta})$  with  $N_g = \varepsilon N_a$  can be made to eliminate  $N_g$  from this expression, which adds a constant factor of  $-N N_a \ln \varepsilon$  to the negative log-likelihood. This choice is optional, but it can be helpful from a computational/organizational standpoint when it comes to projecting the fitted model back onto each Monte Carlo dataset and is chosen in this analysis to give us

$$-2 \ln \mathcal{L}(\vec{\beta}) = -2 \left( \sum_{i=1}^N \left[ w_i \ln \mathcal{I}_i(\vec{\beta}) \right] - \frac{1}{N_a} \sum_{i=j}^{N_a} \left[ w_j \mathcal{I}_j(\vec{\beta}) \right] \right) \quad (4.14)$$

We can now choose a minimization algorithm to fit our data to various models which will be described in detail in [Sections 4.2 and 4.3](#). For this analysis, fits were performed with `laddu`, an amplitude analysis engine I wrote, which uses the L-BFGS-B minimization algorithm, a memory-efficient variant of the Broyden-Fletcher-Goldfarb-Shanno algorithm which allows for box constraints on the parameter space [65].

To obtain plots of the fitted model, we can weight each event in either the accepted or generated Monte Carlo (for results without and with efficiency correction, respectively) as follows,

$$\hat{w}_j = \frac{w_j \mathcal{I}_j(\vec{\beta}^*)}{N_{MC}} \quad (4.15)$$

where  $\vec{\beta}^*$  is the value of the fit parameters which maximizes the likelihood and  $N_{MC}$  is  $N_a$  or  $N_g$  depending on which set of Monte Carlo we are using. We can additionally isolate individual waves by manually setting the coefficients of other waves to zero before evaluating the intensity.

---

<sup>1</sup>This is not to be confused with  $\mathcal{I}_i(\vec{\beta})$ , which we will use to refer to the function evaluated over data. These terms will always stay in separate sums for clarity.

## Uncertainty Estimation

Quasi-Newton minimization algorithms like L-BFGS-B<sup>2</sup> perform gradient descent by making progressively better estimations of the Hessian matrix  $\mathbf{H}$  at each step in the algorithm. One can then obtain an estimate of the uncertainty of the parameter  $\beta_i$  from  $\sigma = \sqrt{(\mathbf{H}^{-1})_{ii}}$ , for which we can either use the Hessian approximate at the end of the minimization or calculate the true Hessian to some arbitrary level of computational precision using finite differences. However, neither method tells us any further detail about the shape of the likelihood surface at the minimum other than the standard deviation of a particular parameter. To examine higher order moments, we require methods which either directly sample the parameter space, e.g. Markov chain Monte Carlo (MCMC), or which resample the data, e.g. the jackknife or bootstrap methods. For this thesis, we will use the bootstrap, as MCMC methods are much more time-consuming and require the tuning of hyperparameters and walker steps, and the jackknife method, which involves resampling the data by omitting one or more events at a time, is only preferred when the bootstrap method described as follows is computationally infeasible.

The bootstrap method derives from the following reasoning. If we had some existing estimate of uncertainty, we could check the estimate by simply collecting more data, performing the analysis on this new data, and observing if our results fall within the estimated uncertainty. However, even if we were to obtain more data, we lack the original estimate of uncertainty. We can obtain such an estimate by “pulling ourselves up by our bootstraps” and resampling the data with replacement to obtain a slightly different “bootstrapped” dataset, which has the same number of events as the original, but contains some duplicate events and misses some of the original events. Assuming the original data is a representative sample of our population (in this case, assuming a new set of data would only effect the precision of our results), we can obtain several of these bootstrapped datasets and perform our fit. We must start each fit at the true minimum found from the original dataset, since we want to understand the uncertainty as it relates to our model, not to the path the minimizer takes, which may run into different local/false minima in each bootstrapped dataset. The distribution of a parameter over many bootstrapped analyses can then be associated with the uncertainty of that parameter.

We begin by defining the statistic  $\hat{\beta}_i(X) = \beta_i^*$  where  $X$  represents the dataset and  $\hat{\beta}_i$  is the maximum likelihood estimator of  $\beta_i$  which maps the events in the dataset to a particular value  $\beta_i^*$  via the fitting process we described in [Section 4.1](#). We then resample the data with replacement  $B$  times to obtain bootstrapped datasets  $\{X_1, \dots, X_b\}$ . The standard error on the parameter  $\beta_i$  is then given by [66],

$$\hat{\sigma}_{\beta_i}^{(B)} = \sqrt{\sum_{b=1}^B \frac{\left(\hat{\beta}_i(X_b) - \frac{1}{B} \sum_{b'=1}^B \hat{\beta}_i(X_{b'})\right)^2}{B-1}} \quad (4.16)$$

---

<sup>2</sup>This also applies to other algorithms commonly used in this field, like MINUIT |

We can also extract confidence intervals for each parameter using bootstrapping. These might be more useful than our standard error estimates, since the shape of the likelihood surface is not necessarily symmetric. First, we define the cumulative distribution function of the  $\hat{\beta}_i$  statistic as [66],

$$\text{CDF}_i(t) = \Pr(\hat{\beta}_i < t) = \frac{\#\{\hat{\beta}_i(X_b) < t\}}{B} \quad (4.17)$$

where  $\#\{\cdot\}$  represents the number of values satisfying the enclosed condition<sup>3</sup>. Then, for some value  $\alpha \in [0, 1]$ , we define

$$\hat{\theta}_i(\alpha) \equiv \text{CDF}_i^{-1}(\alpha) \quad (4.18)$$

We then define the  $(1 - 2\alpha) \cdot 100\%$  central confidence interval for  $\beta_i$  as  $\beta_i \in [\hat{\theta}(\alpha), \hat{\theta}(1 - \alpha)]$ . Furthermore, we can define a bias-corrected confidence interval [66] which corrects for the fact that the mean of the bootstrap distribution is not necessarily the value obtained from the fit to the original data. First, we define a bias-correction factor,

$$z_0 = \Phi^{-1}\left(\text{CDF}_i(\hat{\beta}_i(X))\right) \quad (4.19)$$

where  $\Phi(z)$  is the cumulative distribution function of the standard normal distribution and  $\hat{\beta}_i(X)$  is the value of  $\beta_i$  we obtain from the fit to the original dataset  $X$ . Then, the bias-corrected  $(1 - 2\alpha) \cdot 100\%$  central confidence interval is  $\beta_i \in [\hat{\theta}(\alpha_{\text{lo}}), \hat{\theta}(\alpha_{\text{hi}})]$  where

$$\alpha_{\text{lo}} = \Phi(2z_0 + z(\alpha)) \quad (4.20)$$

$$\alpha_{\text{hi}} = \Phi(2z_0 + z(1 - \alpha)) \quad (4.21)$$

$$z(\alpha) \equiv \Phi^{-1}(\alpha) \quad (4.22)$$

The interpretation of a confidence interval obtained this way is frequentist: If we were to repeat the GlueX experiment many times and evaluated  $\beta_i$  for each experiment, we would expect  $P\%$  of the values to fall within an  $P\%$  confidence interval. The Bayesian approach would be to assign a “credible interval”, where the probability that an estimate falls in the credible interval is  $P\%$ .

---

<sup>3</sup>The last equality here only holds in the limit as  $B \rightarrow \infty$ , but we will ignore this for now.

## **4.2 Mass-Independent Fits**

## **4.3 Mass-Dependent Fits**

## **4.4 Systematics**

## **Chapter 5**

## **Conclusion**





# Bibliography

- [1] Aristotle. *Metaphysics*. Trans. by W. D. Ross. 1.4,985b10-15. type: classic. URL: <http://classics.mit.edu/Aristotle/metaphysics.html>.
- [2] Aristotle. *Physics*. Trans. by R. P. Hardie and R. K. Gaye. 6.1-3,231a21-234b10. URL: <http://classics.mit.edu/Aristotle/physics.html>.
- [3] John Dalton. *A New System of Chemical Philosophy*. In collab. with Smithsonian Libraries. Manchester: Printed by S. Russell for R. Bickerstaff, Strand, London, 1808. 248 pp. URL: <http://archive.org/details/newssystemofchemi11dalton> (visited on 06/12/2024).
- [4] J. J. Thomson. “Cathode Rays”. In: *Philosophical Magazine* 44 (1897), pp. 293–316.
- [5] J. J. Thomson. *The Corpuscular Theory of Matter*. Scribner’s Sons, New York, 1907.
- [6] E. Rutherford. “LXXIX. The scattering of  $\alpha$  and  $\beta$  particles by matter and the structure of the atom”. In: *The London, Edinburgh, and Dublin Philosophical Magazine and Journal of Science* 21.125 (May 1, 1911). Publisher: Taylor & Francis \_eprint: <https://doi.org/10.1080/14786440508637080>, pp. 669–688. ISSN: 1941-5982. DOI: [10.1080/14786440508637080](https://doi.org/10.1080/14786440508637080). URL: <https://doi.org/10.1080/14786440508637080> (visited on 06/12/2024).
- [7] Orme Masson. “XXIV. The constitution of atoms”. In: *The London, Edinburgh, and Dublin Philosophical Magazine and Journal of Science* 41.242 (Feb. 1, 1921). Publisher: Taylor & Francis \_eprint: <https://doi.org/10.1080/14786442108636219>, pp. 281–285. ISSN: 1941-5982. DOI: [10.1080/14786442108636219](https://doi.org/10.1080/14786442108636219). URL: <https://doi.org/10.1080/14786442108636219> (visited on 06/12/2024).
- [8] J. Chadwick. “Possible Existence of a Neutron”. In: *Nature* 129.3252 (Feb. 1932). Publisher: Nature Publishing Group, pp. 312–312. ISSN: 1476-4687. DOI: [10.1038/129312a0](https://doi.org/10.1038/129312a0). URL: <https://www.nature.com/articles/129312a0> (visited on 06/12/2024).
- [9] M. Gell-Mann. “A schematic model of baryons and mesons”. In: *Physics Letters* 8.3 (Feb. 1, 1964), pp. 214–215. ISSN: 0031-9163. DOI: [10.1016/S0031-9163\(64\)92001-3](https://doi.org/10.1016/S0031-9163(64)92001-3). URL: <https://www.sciencedirect.com/science/article/pii/S0031916364920013> (visited on 06/12/2024).

- [10] G. Aad et al. “Observation of a new particle in the search for the Standard Model Higgs boson with the ATLAS detector at the LHC”. In: *Physics Letters B* 716.1 (Sept. 17, 2012), pp. 1–29. ISSN: 0370-2693. DOI: [10 . 1016/j.physletb.2012.08.020](https://doi.org/10.1016/j.physletb.2012.08.020). URL: <https://www.sciencedirect.com/science/article/pii/S037026931200857X> (visited on 06/12/2024).
- [11] Kenneth G. Wilson. “Confinement of quarks”. In: *Physical Review D* 10.8 (Oct. 15, 1974). Publisher: American Physical Society, pp. 2445–2459. DOI: [10 . 1103/PhysRevD.10.2445](https://doi.org/10.1103/PhysRevD.10.2445). URL: <https://link.aps.org/doi/10.1103/PhysRevD.10.2445> (visited on 06/12/2024).
- [12] Colin J. Morningstar and Mike Peardon. “Glueball spectrum from an anisotropic lattice study”. In: *Physical Review D* 60.3 (July 7, 1999), p. 034509. ISSN: 0556-2821, 1089-4918. DOI: [10 . 1103 / PhysRevD . 60 . 034509](https://doi.org/10.1103/PhysRevD.60.034509). URL: <https://link.aps.org/doi/10.1103/PhysRevD.60.034509> (visited on 08/30/2024).
- [13] Particle Data Group et al. “Review of Particle Physics”. In: *Progress of Theoretical and Experimental Physics* 2020.8 (Aug. 14, 2020), p. 083C01. ISSN: 2050-3911. DOI: [10 . 1093/ptep/ptaa104](https://doi.org/10.1093/ptep/ptaa104). URL: <https://academic.oup.com/ptep/article/doi/10.1093/ptep/ptaa104/5891211> (visited on 08/30/2024).
- [14] S. Adhikari et al. “The GlueX beamline and detector”. In: *Nuclear Instruments and Methods in Physics Research Section A: Accelerators, Spectrometers, Detectors and Associated Equipment* 987 (Jan. 2021), p. 164807. ISSN: 01689002. DOI: [10 . 1016/j.nima.2020.164807](https://doi.org/10.1016/j.nima.2020.164807). URL: <https://linkinghub.elsevier.com/retrieve/pii/S0168900220312043> (visited on 08/30/2024).
- [15] M. Acciarri et al. “ $\{K_S^0 K_S^0\}$  final state in two-photon collisions and implications for glueballs”. In: *Physics Letters B* 501.3 (Mar. 8, 2001), pp. 173–182. ISSN: 0370-2693. DOI: [10 . 1016/S0370-2693\(01\)00116-2](https://doi.org/10.1016/S0370-2693(01)00116-2). URL: <https://www.sciencedirect.com/science/article/pii/S0370269301001162> (visited on 01/31/2025).
- [16] Vincent Mathieu, Nikolai Kochelev, and Vicente Vento. “The physics of glueballs”. In: *International Journal of Modern Physics E* 18.1 (Jan. 2009). Publisher: World Scientific Publishing Co., pp. 1–49. ISSN: 0218-3013. DOI: [10 . 1142/S0218301309012124](https://doi.org/10.1142/S0218301309012124). URL: <https://www.worldscientific.com/doi/abs/10.1142/S0218301309012124> (visited on 01/31/2025).
- [17] The CLAS Collaboration et al. “Double  $\{K_S^0\}$  photoproduction off the proton at CLAS”. In: *Physical Review C* 97.2 (Feb. 26, 2018). Publisher: American Physical Society, p. 025203. DOI: [10 . 1103/PhysRevC.97.025203](https://doi.org/10.1103/PhysRevC.97.025203). URL: <https://link.aps.org/doi/10.1103/PhysRevC.97.025203> (visited on 01/30/2025).

- [18] E. Crémieu-Alcan, Paul Falk-Vairant, and O. Lebey, eds. *Proceedings, Conférence Internationale d'Aix-en-Provence sur les Particules Élémentaires: Aix-en-Provence, France, Sep 14-20, 1961*. Gif-sur-Yvette, France: CEN, 1962.
- [19] A. R. Erwin et al. “Experimental Cross Section for  $\pi\pi\rightarrow\overline{K}K$ ”. In: *Physical Review Letters* 9.1 (July 1, 1962). Publisher: American Physical Society, pp. 34–36. doi: [10.1103/PhysRevLett.9.34](https://link.aps.org/doi/10.1103/PhysRevLett.9.34). URL: <https://link.aps.org/doi/10.1103/PhysRevLett.9.34> (visited on 01/31/2025).
- [20] Gideon Alexander et al. “Final-State Interactions in the  $\pi^+\pi^0\rightarrow K^+\overline{K}^0$  Reaction”. In: *Physical Review Letters* 9.11 (Dec. 1, 1962). Publisher: American Physical Society, pp. 460–464. doi: [10.1103/PhysRevLett.9.460](https://link.aps.org/doi/10.1103/PhysRevLett.9.460). URL: <https://link.aps.org/doi/10.1103/PhysRevLett.9.460> (visited on 01/31/2025).
- [21] David J. Crennell et al. “Observation of an Enhancement in the  $I=0$   $\{K_{-1}^0\}\{K_{-1}^0\}$  System at 1068 MeV”. In: *Physical Review Letters* 16.22 (May 30, 1966). Publisher: American Physical Society, pp. 1025–1029. doi: [10.1103/PhysRevLett.16.1025](https://link.aps.org/doi/10.1103/PhysRevLett.16.1025). URL: <https://link.aps.org/doi/10.1103/PhysRevLett.16.1025> (visited on 01/31/2025).
- [22] Richard I. Hess et al. “Low-Mass  $\overline{K}K$  Systems Produced in  $\pi^+\pi$  Interactions Below 5 BeV/c”. In: *Physical Review Letters* 17.21 (Nov. 21, 1966). Publisher: American Physical Society, pp. 1109–1112. doi: [10.1103/PhysRevLett.17.1109](https://link.aps.org/doi/10.1103/PhysRevLett.17.1109). URL: <https://link.aps.org/doi/10.1103/PhysRevLett.17.1109> (visited on 01/31/2025).
- [23] Orin I. Dahl et al. “Strange-Particle Production in  $\pi^+\pi$  Interactions from  $1.5$  to  $4.2$   $\frac{\text{BeV}}{c}$ . I. Three-and-More-Body Final States”. In: *Physical Review* 163.5 (Nov. 25, 1967). Publisher: American Physical Society, pp. 1377–1429. doi: [10.1103/PhysRev.163.1377](https://link.aps.org/doi/10.1103/PhysRev.163.1377). URL: <https://link.aps.org/doi/10.1103/PhysRev.163.1377> (visited on 01/31/2025).
- [24] W. Beusch et al. “Observation of resonance in the  $K^0\overline{K}^0$  system”. In: *Physics Letters B* 25.5 (Sept. 18, 1967), pp. 357–361. ISSN: 0370-2693. doi: [10.1016/0370-2693\(67\)90095-0](https://www.sciencedirect.com/science/article/pii/0370269367900950). URL: <https://www.sciencedirect.com/science/article/pii/0370269367900950> (visited on 01/31/2025).
- [25] T. F. Hoang et al. “ $K_{-1}^0\overline{K}_{-1}^0\rightarrow K_{-1}^0\overline{K}_{-1}^0$  Threshold Enhancement in  $\pi^+\pi\rightarrow K_{-1}^0\overline{K}_{-1}^0$  at 4 and 5 GeV/c”. In: *Physical Review Letters* 21.5 (July 29, 1968). Publisher: American Physical Society, pp. 316–319. doi: [10.1103/PhysRevLett.21.316](https://link.aps.org/doi/10.1103/PhysRevLett.21.316). URL: <https://link.aps.org/doi/10.1103/PhysRevLett.21.316> (visited on 01/31/2025).

- [26] T.F. Hoang et al. “Investigation of  $\pi^+p \rightarrow K_1^+K_1^0$  at 4 and 5 GeV/c”. In: *Physical Review* 184.5 (Aug. 25, 1969). Publisher: American Physical Society, pp. 1363–1374. DOI: [10.1103/PhysRev.184.1363](https://link.aps.org/doi/10.1103/PhysRev.184.1363). URL: <https://link.aps.org/doi/10.1103/PhysRev.184.1363> (visited on 01/31/2025).
- [27] W. Beusch et al. “A new upper limit for the decay rate ( $f \rightarrow \pi^0$ )”. In: *Physics Letters B* 60.1 (Dec. 22, 1975), pp. 101–104. ISSN: 0370-2693. DOI: [10.1016/0370-2693\(75\)90539-0](https://www.sciencedirect.com/science/article/pii/0370269375905390). URL: <https://www.sciencedirect.com/science/article/pii/0370269375905390> (visited on 01/31/2025).
- [28] W. Wetzel et al. “A study of  $p \rightarrow K^0K^0$  using an experiment on  $p \rightarrow K^0K^0$  at 8.9 GeV/c”. In: *Nuclear Physics B* 115.2 (Nov. 22, 1976), pp. 208–236. ISSN: 0550-3213. DOI: [10.1016/0550-3213\(76\)90254-6](https://www.sciencedirect.com/science/article/pii/0550321376902546). URL: <https://www.sciencedirect.com/science/article/pii/0550321376902546> (visited on 01/31/2025).
- [29] N. M. Cason et al. “Observation of a New Scalar Meson”. In: *Physical Review Letters* 36.25 (June 21, 1976). Publisher: American Physical Society, pp. 1485–1488. DOI: [10.1103/PhysRevLett.36.1485](https://link.aps.org/doi/10.1103/PhysRevLett.36.1485). URL: <https://link.aps.org/doi/10.1103/PhysRevLett.36.1485> (visited on 01/30/2025).
- [30] V. A. Polychronakos et al. “Study of the reaction  $\pi^+p \rightarrow nK^+K^0$  at 6.0 and 7.0 GeV/c”. In: *Physical Review D* 19.5 (Mar. 1, 1979). Publisher: American Physical Society, pp. 1317–1335. DOI: [10.1103/PhysRevD.19.1317](https://link.aps.org/doi/10.1103/PhysRevD.19.1317). URL: <https://link.aps.org/doi/10.1103/PhysRevD.19.1317> (visited on 01/31/2025).
- [31] F. Barreiro et al. “Production and decay properties of  $f(1514)$  in  $Kp$  interactions at 4.2 GeV/c”. In: *Nuclear Physics B* 121.2 (Apr. 4, 1977), pp. 237–250. ISSN: 0550-3213. DOI: [10.1016/0550-3213\(77\)90436-9](https://www.sciencedirect.com/science/article/pii/0550321377904369). URL: <https://www.sciencedirect.com/science/article/pii/0550321377904369> (visited on 01/31/2025).
- [32] S. R. Gottesman et al. “Peripheral production and decay of  $K_S^0K_S^0$  in the reaction  $\pi^+p \rightarrow K_S^0K_S^0 + \text{neutrals}$  at 15.4 GeV/c”. In: *Physical Review D* 22.7 (Oct. 1, 1980). Publisher: American Physical Society, pp. 1503–1512. DOI: [10.1103/PhysRevD.22.1503](https://link.aps.org/doi/10.1103/PhysRevD.22.1503). URL: <https://link.aps.org/doi/10.1103/PhysRevD.22.1503> (visited on 01/30/2025).
- [33] A. Etkin et al. “Amplitude analysis of the  $K_S^0K_S^0$  system produced in the reaction  $\pi^+p \rightarrow K_S^0K_S^0n$  at 23 GeV/c”. In: *Physical Review D* 25.7 (Apr. 1, 1982). Publisher: American Physical Society, pp. 1786–1802. DOI: [10.1103/PhysRevD.25.1786](https://link.aps.org/doi/10.1103/PhysRevD.25.1786). URL: <https://link.aps.org/doi/10.1103/PhysRevD.25.1786> (visited on 01/31/2025).

- [34] M. Althoff et al. “Production of  $KK$ -pairs in photon-photon collisions and the excitation of the tensor meson  $f(1515)$ ”. In: *Physics Letters B* 121.2 (Jan. 27, 1983), pp. 216–222. ISSN: 0370-2693. DOI: [10.1016/0370-2693\(83\)90917-6](https://doi.org/10.1016/0370-2693(83)90917-6). URL: <https://www.sciencedirect.com/science/article/pii/0370269383909176> (visited on 01/30/2025).
- [35] R. S. Longacre et al. “A measurement of  $p \rightarrow K_0^* K_0^* n$  at 22 GeV/c and a systematic study of the  $2^{++}$  meson spectrum”. In: *Physics Letters B* 177.2 (Sept. 11, 1986), pp. 223–227. ISSN: 0370-2693. DOI: [10.1016/0370-2693\(86\)91061-0](https://doi.org/10.1016/0370-2693(86)91061-0). URL: <https://www.sciencedirect.com/science/article/pii/0370269386910610> (visited on 01/31/2025).
- [36] Christoph Berger et al. “Tensor Meson Excitation in the Reaction  $\gamma \gamma \rightarrow K^0_S K^0_S$ ”. In: *Z. Phys. C* 37 (1988), p. 329. DOI: [10.1007/BF01578125](https://doi.org/10.1007/BF01578125).
- [37] D. Aston et al. “A study of the  $K_S^0 K_S^0$  system in the reaction  $K p \rightarrow K_S^0 K_S^0$  at 11 GeV/c”. In: *Nuclear Physics B* 301.4 (May 16, 1988), pp. 525–553. ISSN: 0550-3213. DOI: [10.1016/0550-3213\(88\)90276-3](https://doi.org/10.1016/0550-3213(88)90276-3). URL: <https://www.sciencedirect.com/science/article/pii/0550321388902763> (visited on 01/31/2025).
- [38] H. -J. Behrend et al. “The  $K_S^0 K_S^0$  final state in  $\pi^+ \pi^-$  interactions”. In: *Zeitschrift für Physik C Particles and Fields* 43.1 (Mar. 1, 1989), pp. 91–96. ISSN: 1431-5858. DOI: [10.1007/BF02430613](https://doi.org/10.1007/BF02430613). URL: <https://doi.org/10.1007/BF02430613> (visited on 01/31/2025).
- [39] M. Acciarri et al. “Study of the  $K_S^0 K_S^0$  final state in two-photon collisions”. In: *Physics Letters B* 363.1 (Nov. 16, 1995), pp. 118–126. ISSN: 0370-2693. DOI: [10.1016/0370-2693\(95\)01041-N](https://doi.org/10.1016/0370-2693(95)01041-N). URL: <https://www.sciencedirect.com/science/article/pii/037026939501041N> (visited on 01/31/2025).
- [40] M. A. Reyes et al. “Partial Wave Analysis of the Centrally Produced  $[K_S^0 K_S^0]$  System at  $\sqrt{s} = 800$  GeV”. In: *Physical Review Letters* 81.19 (Nov. 9, 1998). Publisher: American Physical Society, pp. 4079–4082. DOI: [10.1103/PhysRevLett.81.4079](https://doi.org/10.1103/PhysRevLett.81.4079). URL: <https://link.aps.org/doi/10.1103/PhysRevLett.81.4079> (visited on 01/31/2025).
- [41] B. P. Barkov et al. “Discovery of a narrow resonance state of the system  $K_S^0 K_S^0$  at mass 1520 MeV”. In: *Journal of Experimental and Theoretical Physics Letters* 70.4 (Aug. 1, 1999), pp. 248–253. ISSN: 1090-6487. DOI: [10.1134/1.568160](https://doi.org/10.1134/1.568160). URL: <https://doi.org/10.1134/1.568160> (visited on 01/31/2025).
- [42] G. D. Tikhomirov et al. “Resonances in the  $K_S^0 K_S^0$  system produced in collisions of negative pions with a carbon target at a momentum of 40 GeV”. In: *Physics of Atomic Nuclei* 66.5 (May 1, 2003), pp. 828–835. ISSN: 1562-692X. DOI: [10.1134/1.1576456](https://doi.org/10.1134/1.1576456). URL: <https://doi.org/10.1134/1.1576456> (visited on 01/31/2025).

- [43] V. A. Schegelsky et al. “The  $K_0^* SK_0^*$  final state in two-photon collisions and  $SU(3)$  tensor nonets”. In: *The European Physical Journal A - Hadrons and Nuclei* 27.2 (Feb. 1, 2006), pp. 207–212. ISSN: 1434-601X. DOI: [10.1140/epja/i2005-10264-2](https://doi.org/10.1140/epja/i2005-10264-2). URL: <https://doi.org/10.1140/epja/i2005-10264-2> (visited on 01/31/2025).
- [44] V. V. Vladimirov et al. “Analysis of the  $KSKS$  system from the reaction  $p \rightarrow KSKSn$  at 40 GeV”. In: *Physics of Atomic Nuclei* 69.3 (Mar. 1, 2006), pp. 493–509. ISSN: 1562-692X. DOI: [10.1134/S1063778806030124](https://doi.org/10.1134/S1063778806030124). URL: <https://doi.org/10.1134/S1063778806030124> (visited on 01/30/2025).
- [45] S. Uehara et al. “High-statistics study of  $K_0^* S$  pair production in two-photon collisions”. In: *Progress of Theoretical and Experimental Physics* 2013.12 (Dec. 1, 2013), p. 123C01. ISSN: 2050-3911. DOI: [10.1093/ptep/ptt097](https://doi.org/10.1093/ptep/ptt097). URL: <https://doi.org/10.1093/ptep/ptt097> (visited on 01/31/2025).
- [46] A. Ali et al. “Installation and Commissioning of the GLUEX DIRC”. In: *Journal of Instrumentation* 15.9 (Sept. 2020), p. C09010. ISSN: 1748-0221. DOI: [10.1088/1748-0221/15/09/C09010](https://doi.org/10.1088/1748-0221/15/09/C09010). URL: <https://dx.doi.org/10.1088/1748-0221/15/09/C09010> (visited on 02/06/2025).
- [47] M. Pivk and F.R. Le Diberder. “sPlot: A statistical tool to unfold data distributions”. In: *Nuclear Instruments and Methods in Physics Research Section A: Accelerators, Spectrometers, Detectors and Associated Equipment* 555.1 (Dec. 2005), pp. 356–369. ISSN: 01689002. DOI: [10.1016/j.nima.2005.08.106](https://doi.org/10.1016/j.nima.2005.08.106). URL: <https://linkinghub.elsevier.com/retrieve/pii/S0168900205018024> (visited on 08/30/2024).
- [48] Hans Dembinski et al. “Custom Orthogonal Weight functions (COWs) for event classification”. In: *Nuclear Instruments and Methods in Physics Research Section A: Accelerators, Spectrometers, Detectors and Associated Equipment* 1040 (Oct. 2022), p. 167270. ISSN: 01689002. DOI: [10.1016/j.nima.2022.167270](https://doi.org/10.1016/j.nima.2022.167270). URL: <https://linkinghub.elsevier.com/retrieve/pii/S0168900222006076> (visited on 08/30/2024).
- [49] Hirotugu Akaike. “Information Theory and an Extension of the Maximum Likelihood Principle”. In: *Selected Papers of Hirotugu Akaike*. Ed. by Emanuel Parzen, Kunio Tanabe, and Genshiro Kitagawa. New York, NY: Springer, 1998, pp. 199–213. ISBN: 978-1-4612-1694-0. DOI: [10.1007/978-1-4612-1694-0\\_15](https://doi.org/10.1007/978-1-4612-1694-0_15). URL: [https://doi.org/10.1007/978-1-4612-1694-0\\_15](https://doi.org/10.1007/978-1-4612-1694-0_15) (visited on 02/01/2025).
- [50] Gideon Schwarz. “Estimating the Dimension of a Model”. In: *The Annals of Statistics* 6.2 (Mar. 1978). Publisher: Institute of Mathematical Statistics, pp. 461–464. ISSN: 0090-5364, 2168-8966. DOI: [10.1214/aos/1176344136](https://doi.org/10.1214/aos/1176344136). URL: <https://projecteuclid.org/journals/annals-of-statistics/volume-6/issue-2/Estimating-the-Dimension-of-a-Model/10.1214/aos/1176344136.full> (visited on 02/01/2025).



- [51] V. Mathieu et al. “Moments of angular distribution and beam asymmetries in  $\pi^0$  photoproduction at GlueX”. In: *Physical Review D* 100.5 (Sept. 17, 2019), p. 054017. ISSN: 2470-0010, 2470-0029. DOI: [10.1103/PhysRevD.100.054017](https://doi.org/10.1103/PhysRevD.100.054017). URL: <https://link.aps.org/doi/10.1103/PhysRevD.100.054017> (visited on 03/03/2025).
- [52] G. Breit and E. Wigner. “Capture of Slow Neutrons”. In: *Physical Review* 49.7 (Apr. 1, 1936). Publisher: American Physical Society, pp. 519–531. DOI: [10.1103/PhysRev.49.519](https://doi.org/10.1103/PhysRev.49.519). URL: <https://link.aps.org/doi/10.1103/PhysRev.49.519> (visited on 03/03/2025).
- [53] S. U. Chung et al. “Partial wave analysis in K-matrix formalism”. In: *Annalen der Physik* 507.5 (1995). \_eprint: <https://onlinelibrary.wiley.com/doi/pdf/10.1002/andp.19955070504>, pp. 404–430. ISSN: 1521-3889. DOI: [10.1002/andp.19955070504](https://doi.org/10.1002/andp.19955070504). URL: <https://onlinelibrary.wiley.com/doi/abs/10.1002/andp.19955070504> (visited on 03/03/2025).
- [54] K. L. Au, D. Morgan, and M. R. Pennington. “Meson dynamics beyond the quark model: Study of final-state interactions”. In: *Physical Review D* 35.5 (Mar. 1, 1987). Publisher: American Physical Society, pp. 1633–1664. DOI: [10.1103/PhysRevD.35.1633](https://doi.org/10.1103/PhysRevD.35.1633). URL: <https://link.aps.org/doi/10.1103/PhysRevD.35.1633> (visited on 03/06/2025).
- [55] John M. Blatt and Victor F. Weisskopf. *Theoretical Nuclear Physics*. New York, NY: Springer New York, 1979. ISBN: 978-1-4612-9961-5 978-1-4612-9959-2. DOI: [10.1007/978-1-4612-9959-2](https://doi.org/10.1007/978-1-4612-9959-2). URL: <http://link.springer.com/10.1007/978-1-4612-9959-2> (visited on 03/06/2025).
- [56] Frank von Hippel and C. Quigg. “Centrifugal-Barrier Effects in Resonance Partial Decay Widths, Shapes, and Production Amplitudes”. In: *Physical Review D* 5.3 (Feb. 1, 1972). Publisher: American Physical Society, pp. 624–638. DOI: [10.1103/PhysRevD.5.624](https://doi.org/10.1103/PhysRevD.5.624). URL: <https://link.aps.org/doi/10.1103/PhysRevD.5.624> (visited on 03/06/2025).
- [57] I. J. R. Aitchison. “The  $K$ -matrix formalism for overlapping resonances”. In: *Nuclear Physics A* 189.2 (July 17, 1972), pp. 417–423. ISSN: 0375-9474. DOI: [10.1016/0375-9474\(72\)90305-3](https://doi.org/10.1016/0375-9474(72)90305-3). URL: <https://www.sciencedirect.com/science/article/pii/0375947472903053> (visited on 03/06/2025).
- [58] David J. Wilson et al. “Resonances in coupled  $\pi K$  scattering from lattice QCD”. In: *Physical Review D* 91.5 (Mar. 10, 2015). Publisher: American Physical Society, p. 054008. DOI: [10.1103/PhysRevD.91.054008](https://doi.org/10.1103/PhysRevD.91.054008). URL: <https://link.aps.org/doi/10.1103/PhysRevD.91.054008> (visited on 03/06/2025).
- [59] J. A. Oller and E. Oset. “ $N/D$  description of two meson amplitudes and chiral symmetry”. In: *Physical Review D* 60.7 (Sept. 10, 1999). Publisher: American Physical Society, p. 074023. DOI: [10.1103/PhysRevD.60.074023](https://doi.org/10.1103/PhysRevD.60.074023).

074023. URL: <https://link.aps.org/doi/10.1103/PhysRevD.60.074023> (visited on 03/10/2025).
- [60] J. L. Basdevant and Edmond L. Berger. “Unitary coupled-channel analysis of diffractive production of the  $A_1$  resonance”. In: *Physical Review D* 16.3 (Aug. 1, 1977). Publisher: American Physical Society, pp. 657–678. DOI: 10.1103/PhysRevD.16.657. URL: <https://link.aps.org/doi/10.1103/PhysRevD.16.657> (visited on 03/10/2025).
- [61] J. A. Oller and Ulf-G. Meißner. “Chiral dynamics in the presence of bound states: kaon–nucleon interactions revisited”. In: *Physics Letters B* 500.3 (Feb. 22, 2001), pp. 263–272. ISSN: 0370-2693. DOI: 10.1016/S0370-2693(01)00078-8. URL: <https://www.sciencedirect.com/science/article/pii/S0370269301000788> (visited on 03/10/2025).
- [62] J. H. Reid and N. N. Trofimenkoff. “A generating function for Chew–Mandelstam functions”. In: *Journal of Mathematical Physics* 25.12 (Dec. 1, 1984), pp. 3540–3544. ISSN: 0022-2488. DOI: 10.1063/1.526093. URL: <https://doi.org/10.1063/1.526093> (visited on 03/10/2025).
- [63] M. Albrecht et al. “Coupled channel analysis of  $\bar{p}p \rightarrow \pi^0 \pi^0 \eta$ ,  $\pi^0 \eta \eta$  and  $K^+ K^- \pi^0$  at 900 MeV/c and of  $\pi \pi$  scattering data”. In: *The European Physical Journal C* 80.5 (May 20, 2020), p. 453. ISSN: 1434-6052. DOI: 10.1140/epjc/s10052-020-7930-x. URL: <https://doi.org/10.1140/epjc/s10052-020-7930-x> (visited on 03/03/2025).
- [64] B. Kopf et al. “Investigation of the lightest hybrid meson candidate with a coupled-channel analysis of  $\bar{p}p$ ,  $\pi^- p$  and  $\pi \pi$ -Data”. In: *The European Physical Journal C* 81.12 (Dec. 1, 2021), p. 1056. ISSN: 1434-6052. DOI: 10.1140/epjc/s10052-021-09821-2. URL: <https://doi.org/10.1140/epjc/s10052-021-09821-2> (visited on 03/06/2025).
- [65] Richard H. Byrd et al. “A Limited Memory Algorithm for Bound Constrained Optimization”. In: *SIAM Journal on Scientific Computing* 16.5 (Sept. 1995). Publisher: Society for Industrial and Applied Mathematics, pp. 1190–1208. ISSN: 1064-8275. DOI: 10.1137/0916069. URL: <https://epubs.siam.org/doi/abs/10.1137/0916069> (visited on 03/26/2025).
- [66] Bradley Efron. “Nonparametric standard errors and confidence intervals”. In: *Canadian Journal of Statistics* 9.2 (1981). \_eprint: <https://onlinelibrary.wiley.com/doi/pdf/10.2307/3314608>, pp. 139–158. ISSN: 1708-945X. DOI: 10.2307/3314608. URL: <https://onlinelibrary.wiley.com/doi/abs/10.2307/3314608> (visited on 03/26/2025).